R. Vescovini
Ritz R-Function Method for the Analysis of Variable-Stiffness Plates
AIAA Journal, published online 16/03/2023
doi:10.2514/1.J062702

The Ritz R-Function Method for the Analysis of Variable Stiffness Plates

Riccardo Vescovini*
Polytechnic University of Milan, Milan, 20156, Italy

This paper presents a novel approach for analyzing the free vibration response of variable stiffness panels. A method is proposed herein, which relies upon a combination of the R-functions and the Ritz method. A powerful and peculiar aspect of this approach consists in the possibility of handling any complex geometry with reduced modeling effort and few degrees of freedom to be handled. The so-obtained formulation is of particular interest for the early design studies of plate- and shell-like structures, especially when topological features are of concern. Specifically, the possibility of studying configurations of arbitrary shape with reduced effort is of crucial importance for exploiting the potential offered by composites with non-straight fibers. Exemplary results are presented for structures with different geometries and shapes. The comparison against results from the literature and finite element calculations reveals the potential of the approach as a valuable mean for assisting the design of innovative variable stiffness configurations.

Nomenclature

a, b	plate dimensions, mm
$\mathbf{A}$, $\mathbf{B}$, $\mathbf{D}$, $\mathbf{A}^s$	laminate constitutive law
c	wing profile chord, mm
$\mathbf{c}_{u_k}$, $\mathbf{c}_{\varphi_\alpha}$	Ritz amplitudes
d	rib length, mm
E_{ik}, G_{ik}	orthotropic material elastic properties, MPa
f, F	real-valued function and Boolean companion function
$\mathcal{F}$	functional
h	plate thickness, mm
K	kinetic energy
$\mathbf{K}$, $\mathbf{M}$	stiffness and mass matrices

Presented as Paper 2022-0535 at AIAA Science and Technology Forum and Exposition, AIAA SciTech Forum 2022, San Diego, CA & Virtual, 3–7 January 2022.

*Associate Professor, Department of Aerospace Science and Technology, Via La Masa 34.

$\mathbf{N}$, $\mathbf{M}$, $\mathbf{Q}$	force, shear and moment resultants
$\mathbf{N}^{ik}$	vector of trial functions
$\overline{\mathbf{Q}}^{(k)}$,$\overline{\mathbf{Q}}_{\mathrm{s}}^{(k)}$	ply constitutive laws
R	circle radius, mm
$S_2\,(\cdot)$	binary operator
t	wing profile thickness as fraction of the chord
$\mathbf{u}_0$, $\boldsymbol{\varphi}$	generalized displacements
U	strain energy
β_i	Boolean flags
$\boldsymbol{\varepsilon}$, $\boldsymbol{\gamma}$	direct and transverse strains
$\boldsymbol{\epsilon}$, $\mathbf{k}$	membrane strains and curvatures
θ	fiber orientation angle
ξ, η	nondimensional coordinates
ρ	density, kg/mm^3
Σ_i, σ_i	primitive domain and corresponding real-valued function
$\boldsymbol{\phi}$, $\boldsymbol{\psi}$	vectors of polynomial expansions
Ω, ω	generic domain as composition of primitive ones and corresponding real-valued function
ω_{u_k}, ω_{φ_α}	boundary functions

I. Introduction

The development of fast computational methods has attracted the attention of many researchers in the field of aerospace structures in the years. As a matter of fact, fast methods allow engineers to gather deeper understanding into the problem at hand. This is true both from a theoretical perspective, but also from a practical standpoint: more rapid computational tools allow parametric studies to be conducted with more ease, helping the designer to shed light into the effect of design variables on the structural response of concern. In this spirit, more refined and costly solution methods should not be seen as an alternative to fast methods, but as complementary tools for the design process as a whole.

This is the underlying philosophy adopted by Prof. Johann Arbocz in developing the computer program DISDECO [1, 2] for the postbuckling analysis of composite shells. Indeed, the code embeds a collection of analytical, semi-analytical and numerical methods with increasing levels of complexity. Specifically, the system DISDECO relies upon a 3-level hierarchical analysis approach, where Level-1 analysis, the simplest among the three, includes routines for buckling

analysis based on a limited number of assumed modes. This initial level is developed for the buckling analysis of anisotropic circular cylindrical shells under compression, shear, bending and external pressure. It is a valuable mean for initial estimates, with essentially no time for modeling and fast computation of results. In the framework of a building-block approach, Level 1 is the first step to gather initial knowledge on the shell response. In a subsequent step, Level 2, the effects of nonlinear prebuckling and rigorously enforced boundary conditions can be handled via numerical solution. The approach relies on the Fourier expansion along the circumference and the solution of the corresponding ordinary differential equations along the axial direction. The last step, Level 3, allows advanced geometric and material nonlinearities to be considered and is based on a finite element solution procedure. The three steps are not alternative, but they are complementary each other.

It is then clear that a continuous development of analytical and semi-analytical methods is crucial for supporting the progress in aerospace design towards the next generation structures, exactly as it has been during past decades. In this field, recent applications are found for supporting the design of composite stiffened panels, such as the ones employed in fuselages and wings, to be designed by accounting for buckling and post-buckling requirements [3–5]. Recently, attention has shifted towards the potential offered by variable stiffness (VS) configurations – composite structures whose elastic properties are not constant along the planar directions – to achieve improved structural response due to better shaping of the stiffness distribution [6–9]. The increased number of degrees of freedom offered by a VS design requires appropriate handling, thus the role of fast methods is even more important than it used to be for classical composites. For this reason, a number of fast methods were proposed in the past few years. The literature is relatively vast, but meaningful examples are found in Refs. [10–16].

One common and restricting feature of semi-analytical strategies deals with their applicability to relatively simple configurations, such as rectangular panels or cylindrical shells. An interesting exception is the approach proposed in Ref. [17], where the buckling response of VS panels with circular cutouts is studied by enriching the functions used in the Ritz expansion. However, even this approach is restricted to a specific class of configurations' i.e. rectangular plates with circular cutouts. More complex domains, e.g. panels with non-rectangular shape or different types of opening, can be hardly considered in the proposed framework. In these situations, the common practice refers to the use of more time-consuming strategies, such as FE-based ones. The solution time by itself can be relatively small, but the time for mesh generation should be accounted for, too. As a whole, the FE approach can thus require an amount of time that, especially for preliminary assessments, can be drastically reduced if more advanced semi-analytical strategies are developed.

Aiming at filling this gap, this work presents a fast analysis tool based on the combined use of R-functions and the Ritz method for analyzing the free vibration response of VS panels with arbitrarily complex domains and boundary conditions. Despite the huge potentials offered by R-functions, their spread has been somewhat limited so far. Efforts can be found in applications to isotropic [18–20] and orthotropic panels [21]. The present work appears to be the first

attempt to link R-functions with VS composites, which is quite a natural combination, given the inherent tailoring potential of VS designs especially in the presence of complex configurations.

The work is organized as follows: an introduction is provided to R-functions, plate kinematics and the description of the non-uniform elastic properties in Section II; the Ritz approximation is illustrated in Section III along with a brief discussion on the numerical procedures for the integration and differentiation; the analysis of three test cases is presented in Section IV, while conclusions are reported in Section V.

II. Geometry, Kinematics and Elastic Properties

Variable stiffness panels with arbitrary shapes are the goal of this investigation. In this section, an overview is provided on R-functions, which are used in the context of the Ritz method as the analytical tool for representing the plate geometry. Furthermore, plate kinematics and the description of the non-uniform elastic properties are presented.

A. A Brief on R-functions

A brief introduction is provided here to R-function for the sole scopes of this paper. The topic is discussed thoroughly in Refs. [22–24], to which the interested reader is referred to. A concise yet clear introduction is available also in the book by Amabili [25]. R-functions are a special class of functions due to the Russian mathematician V.L. Rvachev, which offer a drastic potential to simplify the solution of several problems governed by partial differential equations, such as those arising in structural mechanics.

A peculiar aspect of R-functions is that their sign is fully determined by the sign of the arguments, thus relying upon a partition between positive and negative numbers. Other partitions are clearly possible, see [24], but are not considered here.

Given a real-valued function $f = f(x_i)$, where x_i depends upon the problem dimensionality, its Boolean companion function F can be defined as:

$$F\left(S_2(x_i)\right) = S_2\left(f(x_i)\right) \tag{1}$$

where the binary operator S_2 reads:

$$S_2(x_i) = \begin{cases} 0 & x_i < 0 \\ 1 & x_i > 0 \end{cases} \tag{2}$$

Referring to Eq. (1), one can note that F is indeed Boolean as its arguments $S_2(x_i)$ are, and the output is Boolean too, as seen from the right-hand-side of the equation. A very large number of R-functions exists, many of them sharing the same companion function F. Each R-function sharing a common companion function F forms a so-called *branch*.

Dealing with R-functions does not require the ability to build any possible function. On the contrary, it is sufficient to construct at least one R-function per branch. This consideration is known under the notion of *sufficiently complete set*,

which denotes a set with not null intersection with each branch of the R-functions's set. A system h of R-functions is sufficiently complete if the system H of companion Boolean functions is complete [22]. One example of complete Boolean system is given by conjunction $\wedge$ and negation $\neg$. Indeed, these two functions allow any other Boolean function to be constructed.

In the field of R-functions, previous works established the advantages of using other systems of Boolean functions that are complete, see [22–24]. In particular, one choice that proved to be useful and numerically robust consists in choosing the following complete set of functions:

$$\begin{aligned} \overline{x} &= -x && \text{(R-negation } \neg\text{)} \\ x \wedge_\alpha y &= \frac{1}{1+\alpha}\left(x + y - \sqrt{x^2 + y^2 - 2\alpha x y}\right) && \text{(R-conjunction } \wedge\text{)} \\ x \vee_\alpha y &= \frac{1}{1+\alpha}\left(x + y + \sqrt{x^2 + y^2 - 2\alpha x y}\right) && \text{(R-disjunction } \vee\text{)} \end{aligned} \tag{3}$$

where $\alpha = \alpha(x, y)$ can an arbitrary function $-1 < \alpha \leq 1$. The functions in Eq. (3) are R-functions and their companion Boolean functions are reported as well in the parenthesis. Often α is set equal to zero, this choice leading the operators in Eq. (3) to be modified accordingly, and the operators of conjunction and disjunction to be denoted as $\wedge_0$ and $\vee_0$, respectively.

Whenever a logical expression is reported without brackets, the convention adopted here relies on the following hierarchy of precedences for the logical operators: $\neg$, $\wedge$, $\vee$ (and, accordingly, for the R-operators: $\overline{\ }$, $\wedge_\alpha$, $\vee_\alpha$). For example:

$$x \vee_\alpha y \wedge_\alpha z = x \vee_\alpha (y \wedge_\alpha z) \tag{4}$$

Furthermore, when an operand is surrounded by the same operator on both sides, it is assumed that the operand associates to the left, so:

$$x \wedge_\alpha y \wedge_\alpha z = (x \wedge_\alpha y) \wedge_\alpha z \tag{5}$$

Having introduced R-functions and their correspondence with Boolean functions, it is now possible to exploit the technique to specify how domains of arbitrary shape, hereinafter *complex domains* Ω, can be constructed. This operation is conducted through composition of *primitive domains* Σ_i via the operations defined in Eq. (3). In this context, it is useful to recall that R-functions are closed under composition [23], so the composition of R-functions generates functions belonging to the same set. Consider, for instance, the primitive domain Σ_i, whose definition reads:

$$\Sigma_i = S_2\left(\sigma_i(x_j)\right) \tag{6}$$

where $\sigma_i(x_j)$ is the real-valued function defining the primitive domain; following the notation of Rvachev [22],

Σ_i is used here to denote both the Boolean characteristic function and the domain itself. The index j depends on the domain dimensionality, and falls in the range $j = 1, 2$ and $j = 1, 2, 3$ in two- and three-dimensions, respectively. In other words, when the a point x_j falls inside/outside the domain Σ_i, then the real-valued function $\sigma_i(x_j)$ is positive/negative. Observing now that the characteristic functions $\Sigma_i \in B_2\,\{0, 1\}$, it is then possible to use them as the input of a Boolean function F as:

$$\Omega = F(\Sigma_1, \ldots, \Sigma_N) = 1 \tag{7}$$

where F is chosen in order to achieve the desired complex domain Ω which, in turn, can be understood as a Boolean logic function or the domain itself. Another way of looking at Eq. (7) consists in understanding Ω as the domain defined by the inequality involving the real-valued function f via $\omega \equiv f(\sigma_i) \geq 0$, where F is the companion Boolean function of f. Indeed:

$$\Omega = S_2(f(\sigma_i)) = F(S_2(\sigma_i)) \tag{8}$$

Based on the above, the real-valued function representing the domain is:

$$\omega = f(\sigma_i) = f(\sigma_i(x_j)) \tag{9}$$

which is nothing but the R-function corresponding to the Boolean function $F = F(S_2(\sigma_i)) = F(\Sigma_i)$. The result of Eq. (9) will be used hereafter to specify the panel domains as well as constructing the boundary functions for the Ritz approximation. In this regard, the R-functions are not alternative to the complete basis used for expanding the unknown fields – orthogonal polynomials are example of which –, but they are a complementary tool for enforcing kinematic boundary conditions.

B. Definition of the Panel Shape

The formulation is developed for considering two-dimensional plate-like structures. Thus, reference is made henceforth to two-dimensional domains, expressing the plate/shell midsurface. The planar coordinates are defined as x and y and they form a set of orthogonal coordinates, while the axis z is taken according to the right-hand rule.

For clarity, two examples are reported below, illustrating how the framework given by the R-functions can be applied for defining domains of practical interest.

Example 1

As a preliminary example, a rectangular domain with an internal circular cutout is considered. The extensions to other geometries is straightforward, and any other shape can be accounted for by following the same workflow.

The domain has horizontal and vertical dimensions denoted as a and b, respectively. A circular hole of radius R is

considered, whose center has coordinates (x_0, y_0). The definition of the domain is illustrated in Figure 1, where the three primitive domains Σ_1, Σ_2 and Σ_3 are presented in Figures 1(a) to 1(c); the complex domain Ω – in this case, the plate with circular hole – obtained through the composition of the first three primitive ones is available in Figure 1(d). Note, the boundaries to the domains are denoted using the symbol ∂. Based on the notation introduced earlier, σ_i are the real-valued functions defining the elementary domains, while ω is the real-valued function representing the domain Ω.

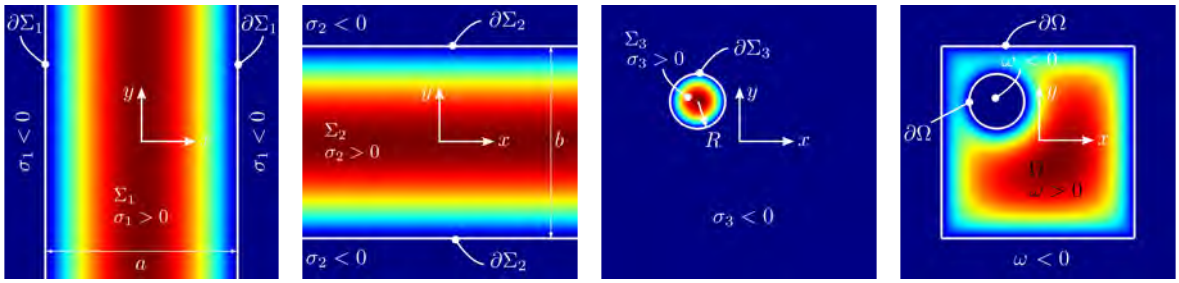

(a) (b) (c) (d)

Fig. 1 Definition of a domain using R-functions: (a) vertical strip, (b) horizontal strip, (c) circular hole, (d) rectangular domain embedding circular hole.

It is straightforward to express the functions σ_i as:

$$\sigma_1 = \frac{a^2 - x^2}{2a}, \quad \sigma_2 = \frac{b^2 - y^2}{2b}, \quad \sigma_3 = \frac{1}{2R}\left[R^2 - (x - x_0)^2 - (y - y_0)^2\right] \tag{10}$$

and the corresponding domains are obtained by application of Eq. (3). The contour plots of the three functions specified by Eq. (10) are displayed in Figures 1(a) to 1(c). From simple geometric considerations, the complex domain Ω can be thought as the following combination of Boolean conjunction operations:

$$\Omega = (\Sigma_1 \wedge \Sigma_2) \wedge \neg\Sigma_3 \tag{11}$$

The R-function ω corresponding to Ω is obtained by replacing the Boolean operations in Eq. (12) with those defined in Eq. (3), and leading to:

$$\omega = \omega(x, y) = (\sigma_1 \wedge_0 \sigma_2) \wedge_0 \overline{\sigma_3} \tag{12}$$

where the functions σ_i are available in Eq. (10). The contour plot of the function expressed by Eq. (12) is reported in Figure 1(d). It is interesting to note that the function $\omega = \omega(x, y)$ is null along the boundary $\partial\Omega$, positive inside the domain and negative outside. These features are particularly useful when developing the numerical procedures discussed next.

Example 2

More complex examples can be easily constructed by following the approach outlined above. As an example, a wing rib can be considered, whose shape can be relatively complex to be handled using the classical tools of structural analysis. Even FEM-based procedure may require relatively costly meshing procedures, which are clearly not desirable when repeated analyses are needed. This example is presented to highlight the ease in defining a relatively complex domain, as well as expressing it as a function of the design variables. It is assumed here that the dimensions of the rib are fixed, while the size and position of inner holes – hereinafter referred to as lightening holes as they are used for structural weight reduction – have to be established during the design iterations. For this reason, the domain is conveniently expressed as a function of these latter parameters.

Starting from the outer shape of the wing profile, a symmetrical NACA four-digits profile is considered. A reference system is considered with the x axis running along the midline. The thicknesswise direction is denoted with y, and the origin of the system is located at the nose of the profile. Based on the previous choices, the outer shapes of the wing profile is described by the functions:

$$\begin{aligned}\sigma_1 &= -y + \left\{5tc\left[0.2969\sqrt{\frac{x}{c}} - 0.1260\frac{x}{c} - 0.3516\left(\frac{x}{c}\right)^2 + 0.2843\left(\frac{x}{c}\right)^3 - 0.1015\left(\frac{x}{c}\right)^4\right]\right\} \\ \sigma_2 &= y + \left\{5tc\left[0.2969\sqrt{\frac{x}{c}} - 0.1260\frac{x}{c} - 0.3516\left(\frac{x}{c}\right)^2 + 0.2843\left(\frac{x}{c}\right)^3 - 0.1015\left(\frac{x}{c}\right)^4\right]\right\}\end{aligned} \tag{13}$$

where c is the chord, while t is the maximum thickness, expressed as a fraction of the chord. The overall length of the rib d is assumed to be smaller with respect to the whole profile, i.e. $d/c < 1$, so the following function can be defined:

$$\sigma_3 = d - x \tag{14}$$

Three lightening holes with radii R_k are introduced at different locations of coordinates $(x_k, 0)$. The equation expressing their shapes is defined analogously to what done in Eq. (10), so:

$$\sigma_{k+3} = \frac{1}{2R_k}\left[R_k^2 - \left(\frac{x - x_k}{c}\right)^2 - y^2\right] \qquad k = 1, 2, 3 \tag{15}$$

The set of functions defined by Eqs. (13)-(15) define the primitive domains $\Sigma_i = B_2(\sigma_i)$, which can be combined via Boolean conjunction operators to obtain the rib domain as:

$$\Omega = \Sigma_1 \wedge \Sigma_2 \wedge \Sigma_3 \wedge \neg\Sigma_4 \wedge \neg\Sigma_5 \wedge \neg\Sigma_6, \tag{16}$$

And, upon replacement of the logical conjunction operator with the R-function one defined in Eq. (3), one obtains

the real-valued function:

$$\omega = \omega(x, y, x_k, R_k) = \sigma_1 \wedge_0 \sigma_2 \wedge_0 \sigma_3 \wedge_0 \overline{\sigma_4} \wedge_0 \overline{\sigma_5} \wedge_0 \overline{\sigma_6}, \tag{17}$$

where dependency over the parameters x_k and R_k is explicitly reported.

The domain specified by Eq. (17) is depicted in Figure 2, where the dark blue regions correspond to negative values of ω, thus representing points falling outside the domain; the boundaries of the domain $\partial\Omega$ are represented by white lines and correspond to the locus of points where $\omega = 0$.

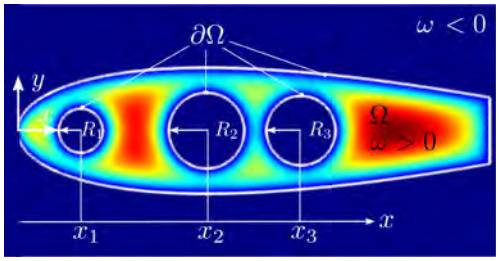

Fig. 2 Rib with lightening holes defined via R-functions.

C. Kinematics

The proposed implementation refers to the First Order Shear Deformation Theory (FDST), whose kinematic description is outlined below for the sake of completeness. Note, the approach is not restricted to a specific kinematic model, but can specialized to case of Classical Lamination Theory (CLT), higher-order models, e.g. Reddy's TSDT [26], or unified theories [27–29] with relative ease.

In the context of FSDT, the displacement field is expressed as:

$$\mathbf{u}(x, y, z) = \begin{bmatrix} \mathbf{I}_3 & z\hat{\mathbf{I}} \end{bmatrix} \begin{Bmatrix} \mathbf{u}_0 \\ \boldsymbol{\varphi} \end{Bmatrix} \tag{18}$$

where $\mathbf{u} = \{u,\ v,\ w\}^{\mathrm{T}}$ is the vector collecting the three components of the displacement field, and:

$$\mathbf{u}_0 = \left\{u_x,\ u_y,\ u_z\right\}^{\mathrm{T}}, \quad \boldsymbol{\varphi} = \left\{\varphi_x,\ \varphi_y\right\}^{\mathrm{T}} \tag{19}$$

are the vectors of the generalized displacement components. Furthermore, $\mathbf{I}_3$ is the identity matrix of order 3, and:

$$\hat{\mathbf{I}} = \begin{bmatrix} 1 & 0 \\ 0 & 1 \\ 0 & 0 \end{bmatrix} \tag{20}$$

The vectors of the strains components are defined as:

$$\begin{aligned}\boldsymbol{\epsilon} &= \left\{\epsilon_{xx},\, \epsilon_{yy},\, \gamma_{xy}\right\}^{\mathrm{T}} = \boldsymbol{\varepsilon} + z\mathbf{k} \\ \boldsymbol{\gamma} &= \left\{\gamma_{yz},\, \gamma_{xz}\right\}^{\mathrm{T}}\end{aligned} \tag{21}$$

where the vectors $\boldsymbol{\varepsilon}$ are the linear membrane strains, $\mathbf{k}$ are the curvatures, whilst $\boldsymbol{\gamma}$ collects the transverse shear components. The corresponding strain-displacement relations are:

$$\boldsymbol{\varepsilon} = \left\{u_{x,x},\, u_{y,y},\, u_{x,y} + u_{y,x}\right\}^{\mathrm{T}}, \quad \mathbf{k} = \left\{\varphi_{x,x},\, \varphi_{y,y},\, \varphi_{x,y} + \varphi_{y,x}\right\}^{\mathrm{T}}, \quad \boldsymbol{\gamma} = \left\{u_{z,y} + \varphi_y,\, u_{z,x} + \varphi_x\right\}^{\mathrm{T}} \tag{22}$$

D. Panel Elastic Properties

Laminated composite panels are of concern, and special focus is given to those configurations characterized by curvilinear fiber paths. Classical, straight-fiber configurations, as well as panels made of isotropic materials can be retrieved as a special case. The panel is assumed to be obtained by the stacking of an arbitrary number of plies, perfectly bonded each other, and characterized by fiber orientations that are a function of the planar position. Among the different possibilities to specify the fiber path – linear variations [7], Lobatto polynomials [30] and piecewise polynomials [31] are examples of which – the approach proposed here relies upon the use of Lagrange polynomials [32, 33]. For each ply, the orientation angles θ_{mn} are provided in a grid of M×N points, and then are interpolated as:

$$\theta(x, y) = \sum_{m=0}^{M-1} \sum_{n=0}^{N-1} \theta_{mn} \prod_{m \neq i} \left(\frac{x - x_i}{x_m - x_i} \right) \prod_{n \neq j} \left(\frac{y - y_j}{y_n - y_j} \right) \tag{23}$$

The description of Eq. (23) allows for a wide variety of configurations to be obtained.
Ply orientations are specified by means of a matrix, whose dimensions correspond to the number of angles specified along the two orthogonal directions. A graphical representation is presented in Figure 3, where the fiber path definition is presented for a panel domain embedding a circular shape.

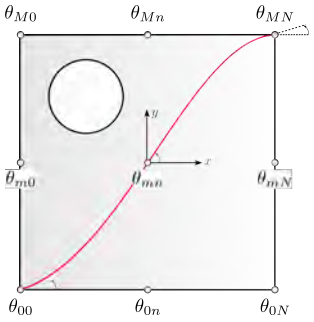

Fig. 3 Fiber path using Lagrange interpolation.

The common case of linearly varying orientations between the panel center and its edge is retrieved by considering two points only. Under these circumstances, the ply is specified as $[\phi < \theta_0 | \theta_1 >]$, where ϕ is the rotation angle around the z axis of the local reference system.

Assuming linear elastic behaviour and plane stress conditions, the stress-strain relation reads:

$$\boldsymbol{\sigma}^{(k)} = \overline{\mathbf{Q}}^{(k)}(x, y)\boldsymbol{\epsilon}^{(k)} \qquad \boldsymbol{\tau}^{(k)} = \overline{\mathbf{Q}}_{\mathrm{s}}^{(k)}(x, y)\boldsymbol{\gamma} \tag{24}$$

where the superscript (k) is introduced to denote the k-th ply composing the laminate; the matrices $\overline{\mathbf{Q}}^{(k)}$ and $\overline{\mathbf{Q}}_{\mathrm{s}}^{(k)}$ are the constitutive law of the ply k in the global reference system; the strain vectors are defined in Eq. (21). It is worth noting that the ply constitutive laws are functions of the planar position via Eq. (23). This dependence is explicitly indicated in Eq. (24).

Referring to the FSDT kinematic model, it is possible to express the laminate constitutive law as:

$$\begin{aligned}
\mathbf{N} &= \int_h \boldsymbol{\sigma}^{(k)} \,\mathrm{d}z \;= \mathbf{A}(x, y)\boldsymbol{\xi} + \mathbf{B}(x, y)\mathbf{k} \\
\mathbf{M} &= \int_h z\boldsymbol{\sigma}^{(k)} \,\mathrm{d}z \;= \mathbf{B}(x, y)\boldsymbol{\xi} + \mathbf{D}(x, y)\mathbf{k} \\
\mathbf{Q} &= \int_h \boldsymbol{\tau}^{(k)} \,\mathrm{d}z \;= \mathbf{A}^{\mathrm{s}}(x, y)\boldsymbol{\gamma}
\end{aligned} \tag{25}$$

where $\mathbf{N}$, $\mathbf{M}$ and $\mathbf{Q}$ are the force, moment and shear resultants obtained via integration along the laminate's thickness direction. The matrices $\mathbf{A}$, $\mathbf{B}$, $\mathbf{D}$ and $\mathbf{A}^{\mathrm{s}}$ on the right-hand side of Eq. (25) are the membrane, coupling, bending and transverse shear stiffness contributions [26, 34], and define the laminate constitutive law, i.e. the relation between generalized forces and strain parameters. Even these matrices are a function of the in-plane position, meaning that the homogenized laminate stiffness properties are different from point to point due to fiber steering.

III. Approximate Solution via Ritz Method

A. Variational Formulation

The formulation presented here allows free vibration problems to be considered, although the extension to static, buckling and free vibrations ir relatively straightforward [33]. The weak-form formulation is developed starting from the Lagrangian function [35]:

$$\mathcal{F} = K - U \tag{26}$$

where U is the strain energy and K the kinetic energy, and the variational statement, i.e. the Hamilton's principle, reads:

$$\delta \int_{t_1}^{t_2} \mathcal{F} \,\mathrm{d}\, t = 0, \qquad \forall\, \delta\mathbf{u}_0,\ \delta\boldsymbol{\varphi} \tag{27}$$

The variational statement of Eq. (27) provides a systematic way for deriving the governing equations, which are nothing but the Euler-Lagrange equations of associated with the functional $\mathcal{F}$. The weak-form approach proposed here is particularly suited for a direct solution of the problem, which is pursued in the next section by referring to the combined use of R-functions and the Ritz method.

The contributions appearing in Eq. (26) are elaborated as [33]:

$$U = \frac{1}{2}\int_\Omega \begin{Bmatrix} \boldsymbol{\varepsilon} \\ \mathbf{k} \\ \boldsymbol{\gamma} \end{Bmatrix}^{\mathrm{T}} \begin{bmatrix} \mathbf{A}(x,y) & \mathbf{B}(x,y) & \mathbf{0} \\ \mathbf{B}(x,y) & \mathbf{D}(x,y) & \mathbf{0} \\ \mathbf{0} & \mathbf{0} & \mathbf{A}^{\mathrm{s}}(x,y) \end{bmatrix} \begin{Bmatrix} \boldsymbol{\varepsilon} \\ \mathbf{k} \\ \boldsymbol{\gamma} \end{Bmatrix} \mathrm{d}\Omega = \frac{1}{2}\int_\Omega \mathbf{e}^{\mathrm{T}}\mathbf{D}_{\mathrm{p}}\mathbf{e}\,\mathrm{d}\Omega \tag{28}$$

where the definitions of $\mathbf{D}_{\mathrm{p}}$ and $\mathbf{e}$ are implicit in Eq. (28).

The kinetic energy is:

$$K = \frac{1}{2}\int_V \dot{\mathbf{u}}\rho\dot{\mathbf{u}}\,\mathrm{d}V \tag{29}$$

where dot denotes derivative with respect to time and ρ is the material density. Upon substitution of Eq. (18) into Eq. (29) one obtains:

$$K = \frac{1}{2}\int_\Omega \begin{Bmatrix} \dot{\mathbf{u}}_0 \\ \dot{\boldsymbol{\varphi}} \end{Bmatrix}^{\mathrm{T}} \int_h \rho \begin{bmatrix} \mathbf{I}_3 & z\hat{\mathbf{I}} \\ z\hat{\mathbf{I}}^{\mathrm{T}} & z^2\hat{\mathbf{I}}^2 \end{bmatrix} \mathrm{d}z \begin{Bmatrix} \dot{\mathbf{u}}_0 \\ \dot{\boldsymbol{\varphi}} \end{Bmatrix} \mathrm{d}\Omega = \frac{1}{2}\int_\Omega \dot{\mathbf{d}}_0^{\mathrm{T}}\mathbf{m}\dot{\mathbf{d}}_0\,\mathrm{d}\Omega \tag{30}$$

where $\mathbf{d}_0 = \left\{\mathbf{u}_0^{\mathrm{T}},\ \boldsymbol{\varphi}^{\mathrm{T}}\right\}^{\mathrm{T}}$, while the mass matrix $\mathbf{m}$ reads:

$$\mathbf{m} = \begin{bmatrix} I_0 & & & I_1 & & \\ & I_0 & & & I_1 & \\ & & I_0 & & & \\ I_1 & & & I_2 & & \\ & I_1 & & & I_2 & \end{bmatrix} \quad \text{with:}\ \ \{I_0,\ I_1,\ I_2\} = \int_h \rho\left\{1,\ z,\ z^2\right\}\,\mathrm{d}z \tag{31}$$

B. Trial Functions

The variational problem, whose general statement is provided by Eqs. (26) and (27), is solved with a direct solution strategy based on the combined use of the Ritz method and the R-functions. Specifically, the Ritz method is employed to transform the differential problem into an algebraic one via expansion of the unknown fields. The Ritz method requires

trial functions to be chosen as part of a complete set and respectful of the essential boundary conditions. Completeness can be guaranteed by using a polynomial expansion. Monomials and Legendre polynomials have been considered for this scope. At the same time, R-functions are exploited to construct boundary functions capable of enforcing the essential boundary conditions, the procedure being completely analogous the one pursued to define the problem domain.

A generic domain is considered, where x and y denote the in-plane coordinates, and the panel is inscribed into a rectangular region $[x_{\min}\ x_{\max}] \times [y_{\min}\ y_{\max}]$.
The generalized displacement components of Eq. (19) are expanded as:

$$\begin{aligned} u_k(x,y) &= \omega_{u_k}(x,y)\left[\boldsymbol{\phi}(x)^{\mathrm{T}} \otimes \boldsymbol{\psi}(y)^{\mathrm{T}}\right]\mathbf{c}_{u_k} \qquad k = x, y, z \\ \varphi_\alpha(x,y) &= \omega_{\varphi_\alpha}(x,y)\left[\boldsymbol{\phi}(x)^{\mathrm{T}} \otimes \boldsymbol{\psi}(y)^{\mathrm{T}}\right]\mathbf{c}_{\varphi_\alpha} \qquad \alpha = x, y \end{aligned} \tag{32}$$

where ω_{u_k} and ω_{φ_α} are the boundary functions associated with u_k and φ_α, respectively. They are constructed depending on the boundary conditions to be imposed which, in general, are different for each single displacement component. The technique for constructing these functions refers to the R-functions theory presented earlier. Any essential condition requiring the function to be zero along a portion or the whole boundary can be obtained through proper combination of primitive geometries. In the case of fully clamped edges, all the displacement components will be set to zero, with boundary functions ω_{u_k} and ω_{φ_α} equal to the function ω representing the panel domain. On the contrary, free edges will not require any special treatment, and boundary functions can be taken equal to the unitary function.

Referring to Eq. (32), the vectors of amplitudes $\mathbf{c}_{u_k}$ and $\mathbf{c}_{\varphi_\alpha}$ are the Ritz unknown amplitudes, while the vectors $\boldsymbol{\phi}$ and $\boldsymbol{\psi}$ collect the polynomial expansion, these latter defined as:

$$\begin{aligned} \boldsymbol{\phi} &= \left\{1,\ \xi,\ \xi^2,\ \ldots,\ \xi^R\right\}^{\mathrm{T}} \qquad \text{with: } \xi = \frac{2x - x_{\min} - x_{\max}}{x_{\max} - x_{\min}} \\ \boldsymbol{\psi} &= \left\{1,\ \eta,\ \eta^2,\ \ldots,\ \eta^S\right\}^{\mathrm{T}} \qquad \text{with: } \eta = \frac{2y - y_{\min} - y_{\max}}{y_{\max} - y_{\min}} \end{aligned} \tag{33}$$

where a number of function R is taken along the direction x, and S along the direction y. The definition above guarantees that the monomials are centered in the intervals $[x_{\min}\ x_{\max}]$ and $[y_{\min}\ y_{\max}]$, while reaching unitary absolute value at the boundaries. While this features is not strictly necessary, it is desirable to guarantee improved conditioning number in the resulting matrices of the discrete problem. It is worth noting that alternative basis can be used for $\boldsymbol{\phi}$ and $\boldsymbol{\psi}$. For instance, an expansion based on Legendre polynomials can be specified as:

$$\begin{aligned} \boldsymbol{\phi} &= \{p_0(\xi),\ p_1(\xi),\ p_2(\xi),\ \ldots,\ p_{R-1}(\xi)\}^{\mathrm{T}} \\ \boldsymbol{\psi} &= \{p_0(\eta),\ p_1(\eta),\ p_2(\eta),\ \ldots,\ p_{S-1}(\eta)\}^{\mathrm{T}} \end{aligned} \tag{34}$$

where p_i are the Legendre polynomials. Note, monomials and Legendre polynomials offer identical spanning capabilities of the functional space, so the results obtained referring to Eqs. (33) and (34) are identical. Owing to the approximation of Eq. (32), the polynomials of Eqs. (33) and (34) do not need to satisfy the problems' kinematic conditions, which are handled via proper definition of the R-functions.

The trial functions of Eq. (32) can be conveniently written using the compact notation below:

$$\begin{aligned} \mathbf{N}^{00} &= (\boldsymbol{\phi} \otimes \boldsymbol{\psi})^{\mathrm{T}} \qquad \mathbf{N}^{11} = (\boldsymbol{\phi}_{,x} \otimes \boldsymbol{\psi}_{,y})^{\mathrm{T}} \\ \mathbf{N}^{10} &= (\boldsymbol{\phi}_{,x} \otimes \boldsymbol{\psi})^{\mathrm{T}} \quad \mathbf{N}^{01} = (\boldsymbol{\phi} \otimes \boldsymbol{\psi}_{,y})^{\mathrm{T}} \end{aligned} \tag{35}$$

where the two superscripts denote the order of the derivative along the x and y direction, respectively. For instance, $\mathbf{N}^{01}$ denotes 0-th order derivative with respect to the first coordinate, x, and first-order derivative with respect to the second coordinate, y. The terms $\mathbf{N}^{ik}$ are row vectors of dimension $1 \times RS$, combining the $R \times S$ expansions of Eq. (33). For instance, the term $\mathbf{N}^{00}$ reads:

$$\begin{aligned} \mathbf{N}^{00} &= \{\phi_1\psi_1,\ \phi_1\psi_2,\ \ldots,\ \phi_1\psi_S,\ \phi_2\psi_1,\ \phi_2\psi_1,\ \ldots,\ \phi_2\psi_S,\ \ldots,\ \phi_R\psi_1,\ \phi_R\psi_1,\ \ldots,\ \phi_R\psi_S\} = \\ &= \left\{1,\ \eta,\ \ldots,\ \eta^S,\ \xi,\ \xi\eta,\ \ldots,\ \xi\eta^S,\ \ldots,\ \xi^R,\ \xi^R\eta,\ \ldots,\ \xi^R\eta^S\right\} \end{aligned} \tag{36}$$

and similarly are organized the other row vectors $\mathbf{N}^{ik}$.

Due to the notation of Eq. (35), the displacement components of Eq. (32) and their derivatives can be expressed in a convenient form as:

$$u_k = \omega_{u_k}\mathbf{N}^{00}\mathbf{c}_{u_k}, \quad u_{k,x} = \left(\omega_{u_k,x}\mathbf{N}^{00} + \omega_{u_k}\mathbf{N}^{10}\right)\mathbf{c}_{u_k}, \quad u_{k,y} = \left(\omega_{u_k,y}\mathbf{N}^{00} + \omega_{u_k}\mathbf{N}^{01}\right)\mathbf{c}_{u_k} \tag{37}$$

and similarly:

$$\varphi_\alpha = \omega_{\varphi_\alpha}\mathbf{N}^{00}\mathbf{c}_{\varphi_\alpha}, \quad \varphi_{\alpha,x} = \left(\omega_{\varphi_\alpha,x}\mathbf{N}^{00} + \omega_{\varphi_\alpha}\mathbf{N}^{10}\right)\mathbf{c}_{\varphi_\alpha}, \quad \varphi_{\alpha,y} = \left(\omega_{\varphi_\alpha,y}\mathbf{N}^{00} + \omega_{\varphi_\alpha}\mathbf{N}^{01}\right)\mathbf{c}_{\varphi_\alpha} \tag{38}$$

The expansions above form the basis of the Ritz approximation of the problem. Indeed, the discrete problem can be obtained upon substitution of Eqs. (37) and (38) into the functional of Eq. (27), such that the differential problem is transformed into an algebraic one. However, before proceeding with the development of the method, it is necessary to clarify how differentiation of the boundary functions is carried out, and how numerical integration is handled.

C. Differentiation and Integration

Boundary Functions and Evaluation of Derivatives

The boundary functions ω_{u_k} and ω_{φ_α} are built analytically following the procedure outlined in Section II.B. Their expression corresponds to the one representing the domain, ω, only if the displacement is set to zero along the whole boundary $\partial\Omega$. However, the displacement components may need or need not to be zero along subportions of the panel boundary. It follows that boundary functions are, in general, different from the function that specifies the whole domain. At the same time, the rules for constructing them are the same outlined earlier: the portion of the boundary $\partial\Omega_i$ where essential conditions are specified can be still constructed via combination of elementary or primitive shapes.

In addition, the evaluation of the relevant energy quantities in Eq. (26) makes it necessary the computation of the first-order derivatives with respect to the coordinates x and y, as reported in Eqs. (37) and (38). Second-order derivatives would be necessary if Classical Lamination Theory were employed, and the approach presented below could still be applied. The differentiation is carried out inspired by the approach employed in the automatic differentiation (sometimes referred to as AUTODIFF), where any arbitrary complex function to be derived is divided into a sequence of elementary operations, and chain rule is applied repeatedly to these operations. This approach leads to the an exact evaluation of the derivatives, with clear advantages on the accuracy and computational effectiveness of the method.

For clarity, an example is provided referring to a generic boundary function ω_{u_k}, assuming that $\omega_{u_k} = \omega$, the latter expressed by Eq. (12). For convenience, the function ω is reported below:

$$\omega(x, y) = (\sigma_1 \wedge_0 \sigma_2) \wedge_0 \sigma_3 = \omega_\square \wedge_0 \sigma_3 \tag{39}$$

where the function $\omega_\square$ has been defined as:

$$\omega_\square = \sigma_1 \wedge_0 \sigma_2 \tag{40}$$

The chain rule can be applied to Eq. (40) to evaluate its derivatives with respect to the coordinates x and y. Specifically:

$$\frac{\partial \omega_\square}{\partial \{x, y\}} = \frac{\partial \omega_\square}{\partial \sigma_1} \frac{\partial \sigma_1}{\partial \{x, y\}} + \frac{\partial \omega_\square}{\partial \sigma_2} \frac{\partial \sigma_2}{\partial \{x, y\}} \tag{41}$$

where the expressions of $\dfrac{\partial \sigma_1}{\partial \{x, y\}}$ and $\dfrac{\partial \sigma_2}{\partial \{x, y\}}$ are readily available from Eq. (10), whilst the partial derivatives with respect to σ_1 and σ_2 stem from the conjunction operation defined in Eq. (3) and read:

$$\frac{\partial \omega_\square}{\partial \sigma_1} = 1 - \sigma_1 \left(\sigma_1^2 + \sigma_2^2\right)^{-1/2}, \quad \frac{\partial \omega_\square}{\partial \sigma_2} = 1 - \sigma_2 \left(\sigma_1^2 + \sigma_2^2\right)^{-1/2} \tag{42}$$

Recalling now Eq. (39),

$$\frac{\partial \omega}{\partial \{x,y\}} = \frac{\partial \omega}{\partial \omega_\square}\frac{\partial \omega_\square}{\partial \{x,y\}} + \frac{\partial \omega}{\partial \sigma_3}\frac{\partial \sigma_3}{\partial \{x,y\}} \tag{43}$$

In the equation above $\dfrac{\partial \omega_\square}{\partial \{x,y\}}$ is available from Eq. (41), while $\dfrac{\partial \sigma_3}{\partial \{x,y\}}$ is readily obtained by taking the first derivative of the third of Eq. (10). The two remaining terms to be derived follow the same rule of Eq. (42), and, in particular, they are:

$$\frac{\partial \omega}{\partial \omega_\square} = 1 - \omega_\square \left(\omega_\square^2 + \sigma_3^2\right)^{-1/2}, \quad \frac{\partial \omega}{\partial \sigma_3} = 1 - \sigma_3 \left(\omega_\square^2 + \sigma_3^2\right)^{-1/2} \tag{44}$$

The final expression reporting the first-order derivatives of the boundary functions is available in Eq. (43). Despite the simplicity of the example illustrated herein, the same approach can be employed for considering any other set of boundary functions. The approach is systematic and can be easily implemented into a computer routine.

Numerical Integration

The development of a Ritz-based procedure relies upon the need of performing surface integrals to obtain the stiffness and mass matrices appearing in the final set of discrete equations. Given the arbitrariness of the domains to be considered, particular care is needed for developing an adequate integration routine. For many problems of structural interest, the domain is rectangular or, to a more general extent, can be mapped to a regular square in the so-called computational domain. In these cases, integration is carried out with relative ease and, sometimes, analytical integration is even possible, see [36].

When arbitrary domains are of interest, alternative strategies are needed. Two of them appear as the most natural ones to be pursued. The first one consists in adopting a Montecarlo quadrature approach: the integrand function is sampled in a relatively large number of points and the integral is approximated as:

$$I = \int_\Omega f(x,y)\,\mathrm{d}A \approx \frac{A}{N_x N_y}\sum_{i,j=1}^{N_x,N_y} f(x_i,x_j) \tag{45}$$

where N_x and N_y are the number of sampling points along the directions x and y, respectively. Pseudo-random number sets can be employed for this scope, as well as distributions based on specific sequences such as Halton or Sobol [31]. This method offers the advantage of a straightforward implementation, but a relatively large number of function evaluation is generally needed to keep the integration error below adequate thresholds.

The second approach, which is the one proposed here, relies upon the definition of a background mesh, analogously to what is commonly done in the context of meshfree methods [37]. In this case, the domain is divided into elements, which are nothing but smaller and simpler domains introduced for quadrature purposes only. Starting from a tentative subdivision of the domain into smaller rectangular patches, a loop is performed to establish if the elements fall inside, outside or partially outside the domain. Note, this operation is straightforward, as the analytical description of the

domain is available. Whenever one element falls outside the domain by an amount larger than a predefined threshold, the sizes of the element are halved. The procedure is repeated up to convergence. This process is clarified by considering a wing rib, as illustrated in Figure 4. Starting from the rectangular domain $[x_{\min}\ x_{\max}] \times [y_{\min}\ y_{\max}]$ where the structure in inscribed, an initial mesh is generated, and the elements associated with negative values of the R-function ω are progressively removed. The iterative process is illustrated by reporting the background mesh at iterations 2, 3 and 4, see Figures 4(a), 4(b) and 4(c). The final subdivision of the domain into smaller four-node patches is presented in

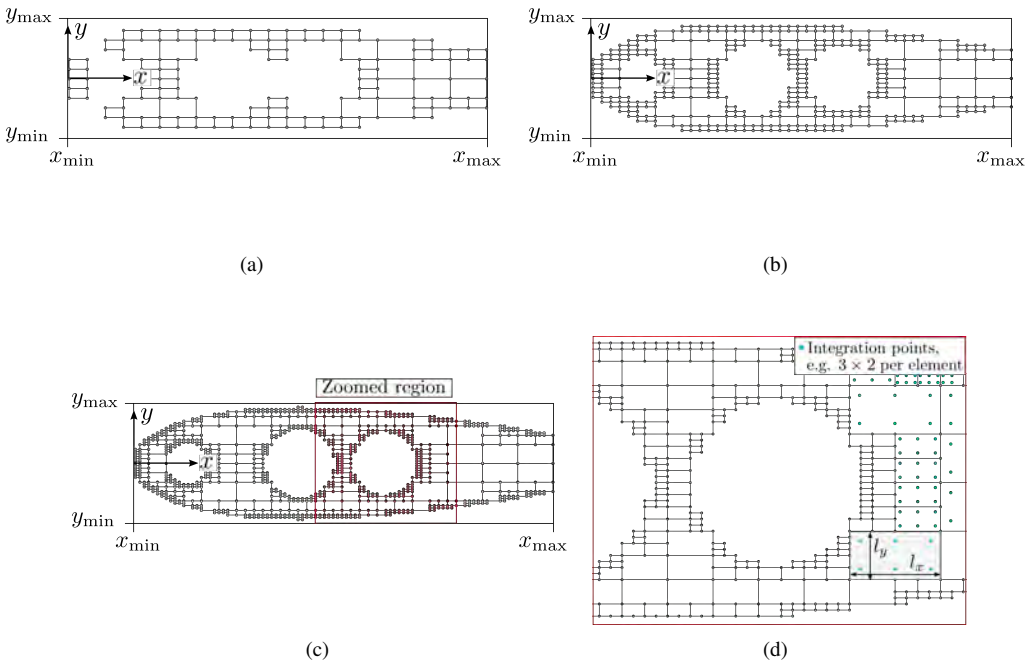

Fig. 4 Background mesh for numerical integration in a wing rib: (a) iteration 2, (b) iteration 3, (c) iteration 4, (d) zoom of a region.

Figure 4(c), the white dots denoting the corners of each single patch. Note that refinement in geometrically complex regions is straightforward, as the size of the patch can be simply halved. No transition mesh is needed as it would for FEM, as patch corners do not need to be coincident.

A zoom is provided in correspondence of the third lightening hole to better show the integration mesh. Each element has dimensions $l_x^{\mathrm{e}} \times l_y^{\mathrm{e}}$ and is provided with a number of Gaussian integration points to be specified as input of the problem. In the example of Figure 4(d), a grid of 3×2 points is considered. Integration is then conducted by using a Gaussian integration scheme by looping over each element composing the background mesh.

D. Discrete Problem

The final set of discrete governing equations arising from the Ritz approximation are obtained upon substitution of Eqs. (37) and (38) into Eq. (26) and are obtained in the form:

$$\left(\mathbf{K} - \omega^2 \mathbf{M}\right) \mathbf{c} = \mathbf{0} \tag{46}$$

where the Ritz amplitudes $\mathbf{c}$ are those referred to all the displacement components and defined as:

$$\mathbf{c} = \left\{ \mathbf{c}_{u_x}^{\mathrm{T}},\, \mathbf{c}_{u_y}^{\mathrm{T}},\, \mathbf{c}_{u_z}^{\mathrm{T}},\, \mathbf{c}_{\varphi_x}^{\mathrm{T}},\, \mathbf{c}_{\varphi_x}^{\mathrm{T}} \right\}^{\mathrm{T}} \tag{47}$$

The matrices appearing in Eq. (46) are obtained by summing the contributions evaluated for each single element composing the background mesh. So:

$$\mathbf{K} = \sum_{e=1}^{N_{\mathrm{e}}} \mathbf{K}^{\mathrm{e}}, \quad \mathbf{M} = \sum_{e=1}^{N_{\mathrm{e}}} \mathbf{M}^{\mathrm{e}} \tag{48}$$

where N_{e} is the total number of elements of the background mesh. Note, unlike in FEM, no assembly procedure is needed: each contribution is already expanded over the total number of degrees of freedom. The matrices corresponding to the whole structure are then obtained by summing up the contributions arising from each single element. The size of the problems is generally small, as relatively few degrees of freedom generally suffice for obtaining a good estimate of the eigenvalues of the problem. It is worth noting that trial functions are defined at global level, so the resulting matrices of Eq. (48) are generally full.

IV. Results

This section illustrates the results obtained using the approach presented earlier. Three test cases are presented to demonstrate the correctness of the implementation along with the potential of the method. The free vibrations response is analyzed for a simple plate, a plate with square cut-out and a rib-like plate structure. Variable stiffness configurations with linearly varying fiber orientation are considered in all the cases.

Example 1

The first example deals with a variable stiffness square plate and is compared against FE results available from the literature, see Ref. [38]. Aim of this example is demonstrating the capability of the proposed approach to deal with non-uniform stiffness properties. Furthermore, the examples aims at validating the correctness of the boundary function implementation via R-function method, along with the relevant procedures of integration and differentiation.

Specifically, the real-valued function expressing the panel's domain is described by the function:

$$\omega = \sigma_1 \wedge_0 \sigma_2 \tag{49}$$

where the expressions for σ_1 and σ_2 are found in Eq. (10). The panel is square with dimension a=1000 mm; two thickness ratios are considered, h/a=0.1 and 0.01. The plate is clamped at the four edges, therefore the boundary functions of Eq. (32) are the same for all the generalized displacement components, i.e. $\omega_{u_k} = \omega_{\varphi_\alpha} = \omega$, as per Eq. (49). The material properties are E_1=173000 MPa, E_2=7200 MPa, G_{12}=G_{13}=G_{23}=3760 MPa and ν_{12}=0.29. The density is ρ=1540 kg/m^3.

Three layups are considered, each characterized by a three-ply symmetric configuration, with the fiber angle varying linearly from the center towards the plate edge. Specifically the layups are:

- L1: $[\langle 0|45\rangle, \langle -45|-60\rangle, \langle 0|45\rangle]$
- L2: $[\langle 30|0\rangle, \langle 45|90\rangle, \langle 30|0\rangle]$
- L3: $[\langle 90|45\rangle, \langle 60|30\rangle, \langle 90|45\rangle]$

The summary of the results is presented in Table 1, where the first four (dimensional) angular frequencies are reported along with the percent differences evaluated with respect to the reference results. For consistency with the reference, the simulations are conducted using 10×10 trial functions for each displacement component, while numerical integration is carried out with a grid of 14 Gaussian integration points distributed over one single element. A shear factor of 5/6 is considered.

Table 1 First four angular frequencies (rad/s) of three VS plates with clamped edges – Comparison against Ref. [38].

		Mode				Mode			
		1	2	3	4	1	2	3	4
Layup		h/a=0.01				h/a=0.1			
L1	Present	579.085	820.971	1225.26	1492.87	3806.42	5689.72	7522.66	8414.30
	Ref. [38]	579.398	821.532	1225.79	1493.76	3856.60	5711.95	7743.34	8406.57
	% diff.	-0.05	-0.07	-0.04	-0.06	-1.30	-0.39	-2.85	0.09
L2	Present	667.731	862.615	1233.63	1700.96	4038.75	5622.03	7823.19	8072.29
	Ref. [38]	667.177	862.919	1234.64	1701.04	4144.85	5696.20	8166.79	8214.53
	% diff.	0.08	-0.04	-0.08	-0.00	-2.56	-1.30	-4.21	-1.73
L3	Present	711.035	912.973	1346.63	1696.68	4170.01	5643.81	7796.76	8037.88
	Ref. [38]	710.771	912.183	1335.49	1689.69	4284.20	5761.83	8193.46	8247.32
	% diff.	0.04	0.09	0.83	0.41	-2.67	-2.05	-4.84	-2.54

It is interesting to note the excellent matching between the present results and the reference ones. This consideration holds particularly true for thin plates, i.e. $h/a = 0.01$, where the differences between the FSDT theory employed here

and the Third Order Shear Deformation Theory (TSDT) presented in Ref. [38] are almost negligible. On the contrary, some slight discrepancies can be noted for thicker plates, i.e. $h/a = 0.1$. This behavior is motivated by the different handling of transverse shear deformation effects between the plate of the present approach – FSDT –, and the one of the referenced work – TSDT.

Example 2

To illustrate the potential of the method in handling more complex shapes, an example is presented regarding a square plate with an inner square hole. The panel is fully clamped, both at the outer edges as well as along the hole. In doing so, trial functions are required to vanish along all over the domain boundaries. Unless R-function theory is used, boundary functions could be hardly obtained.

The panel is characterized by dimension a=150 mm and is made of carbon/epoxy material, whose properties are E_1=147000 MPa, E_2=10300 MPa, G_{12}=G_{13}=G_{23}=7000 MPa and $\nu_{12} = 0.27$, and density $\rho = 1570$ kg/m^3. An eight-ply stacking sequence $[\pm\langle 10|45\rangle]_{2s}$ is considered. The ply thickness is 0.125 mm, corresponding to a total thickness of 1 mm. The square cutout has length b equal to 50 mm and is symmetrically located with respect to the horizontal and vertical axes.

In this case, the background mesh is built by exploiting the geometry of the problem. Specifically, the domain is divided into 8 square subdomains where integration is conducted using a 14 Gauss integration rule. A sketch of the structure is reported in Figure 5(a). The background mesh is depicted in Figure 5(b), where, for clarity, the distribution of integration points is reported at the bottom right for one element composing the background mesh.

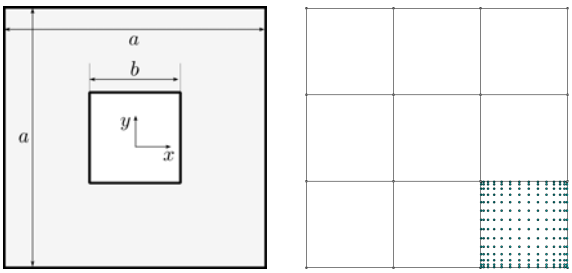

(a) (b)

Fig. 5 VS plate with square cutout: (a) geometry, (b) background mesh.

The Ritz analysis is performed with 26×26 trial functions, defined according to Eq. (32), based on a preliminary convergence study. The boundary functions are specified starting from the elementary domains:

$$\sigma_1 = \frac{a^2 - x^2}{2a}, \quad \sigma_2 = \frac{a^2 - y^2}{2a}, \quad \sigma_3 = \frac{b^2 - x^2}{2b}, \quad \sigma_4 = \frac{b^2 - y^2}{2b} \tag{50}$$

which are combined as:

$$\omega = \omega(x, y) = (\sigma_1 \wedge_0 \sigma_2) \wedge_0 \left(\overline{\sigma_3 \wedge_0 \sigma_4}\right) \tag{51}$$

A comparison is presented against finite element simulations conducted using Abaqus S4R elements, with a mesh density defined according to a preliminary convergence study. The finite element model is realized by assuming constant orientation angles within each element, their values being evaluated at the centroid of the element. The total number of degrees of freedom is slightly above 20,000 for the FEM model, while the Ritz model relies on 3,380 unknowns – 2,028 if the in-plane ones are neglected, as they do not affect the bending vibrations due to uncoupled in-plane and out-of-plane response of the structure under investigation. Hence, the Ritz model is characterized by much smaller dimensions, although the corresponding matrices are, in general, fully populated.

The results are summarized in Figure 6, where the first free vibration modes are reported along with the corresponding dimensional frequencies. Note, only even modes are presented as the symmetry of the problem determines the presence of coupled modes with very close frequencies and similar shapes. The excellent agreement between Abaqus and Ritz

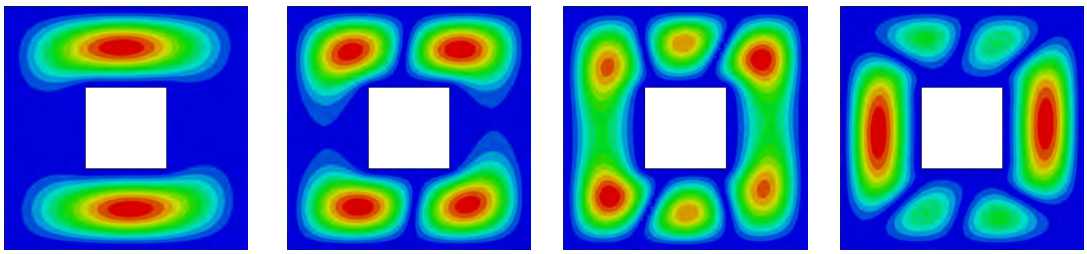

(a) Abaqus, f_1 = 1390.4 Hz (b) Abaqus, f_3 = 1901.6 Hz (c) Abaqus, f_5 = 2563.5 Hz (d) Abaqus, f_7 = 2990.9 Hz

(e) Ritz, f_1 = 1409.4 Hz (f) Ritz, f_3 = 1933.8 Hz (g) Ritz, f_5 = 2576.4 Hz (h) Ritz, f_7 = 2983.4 Hz

Fig. 6 First four mode shapes for VS plate with square hole and clamped along inner and outer boundaries: (a)-(d) Abaqus, (e)-(f) Ritz.

predictions can be noted by inspection of Figure 6. The maximum discrepancy in terms of frequency is smaller than 2%. All the patterns are appropriately predicted despite their relative complexity.

The Ritz-based analytical method allows the solution to be obtained in few seconds. In addition to this, it is worth noting the ease in defining the model when the present approach is used. The position and the size of the hole are parameters of the analytical function ω, and any change to their values does not imply any additional costly remeshing procedure.

Example 3

A third example is reported regarding the analysis of a rib-like structure characterized by non-uniform stiffness properties. The shape of the structure is determined by considering a NACA four-digits profile, with chord equal to 1,000 mm; the maximum thickness, expressed as a fraction of the chord, is 0.275. The length of the rib corresponds to 75% of the total chord length. The material properties are the same presented in *Example 2*, while the stacking sequence is now $[\pm\langle 60|30\rangle/0/90]_{2s}$, corresponding to a total of 16 plies.

The elementary domains are defined according to Eqs. (13) and (14), while the boundary function vanishing along the boundaries is defined through the real-valued function:

$$\omega = \sigma_1 \wedge_0 \sigma_2 \wedge_0 \sigma_3 \tag{52}$$

The effect of different expansions and background meshes is studied for two test cases corresponding to simply-supported and fully clamped outer edges.

The geometry of the structure is reported in Figure 7(a). Two background meshes are considered for the solution of the problem. The first one is obtained starting from an initial seed of 20×10 subdomains, progressively refined until each integration domain falls outside the domain by a maximum of 5 mm^2 (Figure 7(b)). A finer integration mesh is considered where the initial seed is composed 40×20 domains, and the refinement is conducted until the maximum integration area falling outside the domain is equal to 1 mm^2 (Figure 7(c)). A Gauss integration rule with 2 points per subdomain is used.

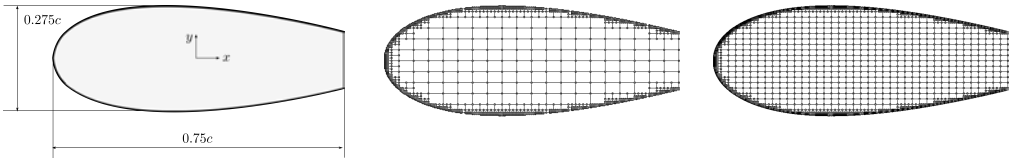

(a) (b) (c)

Fig. 7 Composite plate with cutout: (a) geometry, (b) coarse background mesh, (c) refined background mesh.

As seen, the size of the integration domains gets smaller and smaller in proximity of the boundaries, where relatively small domains are needed to guarantee an accurate integration process. The total number of the elements composing the background meshes is equal to 1,054 and 2,354.

In both cases, the rib shape is appropriately represented. However, the integration process has drastic effects on the accuracy of results, thus apparently minor differences in the integration scheme may affect the results significantly.

The results are summarized in Table 2 for the simply-supported case. Note, the structure is constrained by preventing only the out-of-plane deflections along the boundary, while both the rotations are free. The comparison is reported between the first eight frequencies obtained with the Ritz method and Abaqus finite element simulations.

Table 2 First eight frequencies (Hz) of VS rib with simply-supported edges – Comparison against Abaqus (percent differences are reported as superscripts).

	Ritz				Abaqus
Back. mesh	Coarse (1,054 domains)		Fine (2,354 domains)		
R=S	10×10	14×14	10×10	14×14	
f_1	$95.266^{(-0.00\%)}$	$95.058^{(-0.22\%)}$	$95.459^{(0.20\%)}$	$95.178^{(-0.09\%)}$	95.268
f_2	$140.48^{(-0.06\%)}$	$140.05^{(-0.37\%)}$	$140.86^{(0.21\%)}$	$140.36^{(-0.15\%)}$	140.57
f_3	$203.87^{(0.19\%)}$	$202.54^{(-0.47\%)}$	$204.76^{(0.62\%)}$	$203.03^{(-0.23\%)}$	203.49
f_4	$286.74^{(1.34\%)}$	$281.17^{(-0.63\%)}$	$288.04^{(1.80\%)}$	$281.94^{(-0.36\%)}$	282.96
f_5	$349.33^{(-0.61\%)}$	$349.20^{(-0.65\%)}$	$349.43^{(-0.59\%)}$	$349.31^{(-0.62\%)}$	351.49
f_6	$404.44^{(6.13\%)}$	$378.19^{(-0.76\%)}$	$406.96^{(6.79\%)}$	$379.34^{(-0.46\%)}$	381.08
f_7	$425.54^{(-0.53\%)}$	$424.99^{(-0.65\%)}$	$425.86^{(-0.45\%)}$	$425.30^{(-0.58\%)}$	427.79
f_8	$511.26^{(2.55\%)}$	$495.89^{(-0.53\%)}$	$511.84^{(2.67\%)}$	$496.82^{(-0.35\%)}$	498.54

The results illustrate that lower frequencies are obtained by increasing the number of functions. Given the dependency of the elastic properties with the in-plane coordinates, this conclusion holds true only if the number of integration points is fixed.

The comparison between models with the same expansion but different background meshes reveals that the frequencies tend to increase with the number of integration points. In other words, lower frequencies are obtained by relaxing the integration. This conclusion is not of general validity as it is not necessarily true for any configuration. Indeed, any change in the number of integration points has the effect of sampling the elastic coefficient at different spots.

As seen in Table 2, an expansion with R=S=10 terms and a coarse background mesh are sufficient for providing accurate predictions up to the fifth mode. More functions are needed to appropriately capture higher modes. In particular, when R=S=14, the percent differences between Ritz and Abaqus eigenvalues is smaller than 1% for both the background meshes. It is worth noting that the Ritz frequencies are always smaller than the finite element ones. This behaviour is a consequence of the material nonuniform elastic properties along with the high nonlinearity of the trial functions, which cannot be integrated exactly despite a relatively large number of integration points is used.

In terms of problem size, the Abaqus finite element model is realized with 11,508 degrees of freedom. The Ritz models with 10 and 14 functions require a number of 500 and 980 unknowns, respectively. These numbers reduce to 300 and 588 if restricting the model to the bending-related degrees of freedom only.

The results for fully clamped rib are summarized in Table 3.

The effect of the number of trial functions and integration points on the natural frequency is the same outlined for simply-supported edges. For clamped boundary conditions, the deflected shape requires improved representation capabilities, and an expansion with R=S=14 is necessary to guarantee errors below 2% up to the eight eigenvalue. Accordingly, the need for a larger basis – meaning that the contributions with higher spatial frequency are more relevant – implies the need to integrate using more points. As seen in Table 3, the frequencies can increase up to 2% by switching

Table 3 First eight frequencies (Hz) of VS rib with clamped edges – Comparison against Abaqus (percent differences are reported as superscripts).

	Ritz				Abaqus
Back. mesh	Coarse (1,054 domains)		Fine (2,354 domains)		
R=S	10×10	14×14	10×10	14×14	
f_1	$199.75^{(-2.44\%)}$	$198.14^{(-3.23\%)}$	$202.34^{(-1.18\%)}$	$201.96^{(-1.36\%)}$	204.75
f_2	$247.04^{(-2.43\%)}$	$244.35^{(-3.49\%)}$	$250.30^{(-1.14\%)}$	$249.60^{(-1.41\%)}$	253.18
f_3	$308.86^{(-2.15\%)}$	$304.74^{(-3.45\%)}$	$313.05^{(-0.82\%)}$	$311.28^{(-1.38\%)}$	315.64
f_4	$389.68^{(-1.50\%)}$	$382.91^{(-3.21\%)}$	$394.69^{(-0.23\%)}$	$390.26^{(-1.35\%)}$	395.61
f_5	$522.38^{(5.35\%)}$	$483.32^{(-2.52\%)}$	$529.32^{(6.75\%)}$	$490.34^{(-1.11\%)}$	495.83
f_6	$532.82^{(-1.17\%)}$	$518.23^{(-3.87\%)}$	$538.11^{(-0.19\%)}$	$528.53^{(-1.96\%)}$	539.11
f_7	$608.57^{(-1.39\%)}$	$601.81^{(-2.49\%)}$	$616.69^{(-0.07\%)}$	$610.92^{(-1.01\%)}$	617.15
f_8	$691.64^{(10.20\%)}$	$604.84^{(-3.63\%)}$	$701.74^{(11.81\%)}$	$615.64^{(-1.91\%)}$	627.60

from the coarse to the finer background mesh.

The percent differences between the Ritz model with R=S=14 and fine background mesh and Abaqus results are below 2%. Even in this case the Ritz predictions are associated with slightly smaller eigenvalues with respect to finite element ones.

The plot of the first four eigenmodes is presented in Figure 8, revealing an excellent degree of agreement between numerical and semi-analytical predictions.

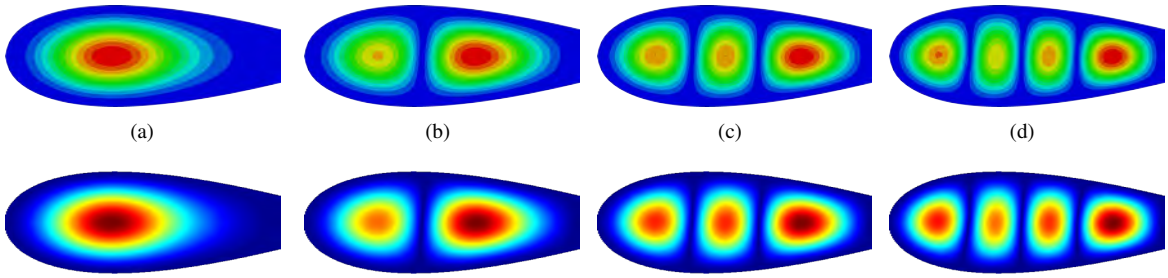

Fig. 8 First four mode shapes for VS rib with clamped edges: (a)-(d) Abaqus, (e)-(f) Ritz.

V. Conclusions

This work presented an approach for the analysis of panels characterized by a combination of complex geometries and non-uniform stiffness properties. The combination of these two aspects is believed of paramount importance to assist the design of variable stiffness structures of the next generation. On one hand, the improved flexibility offered by VS designs makes it crucial the availability of efficient methods for the structural analysis. At the same time, many semi-analytical tools rely upon simplified geometries and do not allow real-life structures to be optimized. This work bridges this gap by combining the efficiency of semi-analytical methods with the possibility of handling structural

configurations that are representative of more realistic applications, a way far from academic test cases relying upon simplified geometries. The use of R-functions allows a wide variety of domains to be generated in a systematic way, while the Ritz method guarantees fast convergence of the solution and an excellent ratio between number of degrees of freedom and accuracy of the solution. The so-developed code is particularly efficient, and is capable of handling thousands of degrees of freedom, while requiring just few seconds for computing the solution. The code is particularly suitable for performing preliminary studies to optimize the stiffness tailoring along with the possibility of handling any topological aspect with great ease.

At the current stage, the implementation has been restricted to the linear free vibrations, but extension to other solution procedures, including the nonlinear ones is the subject of ongoing research activities.

Appendix

A. Preliminary Operations

To allow a compact expressions of the relevant equations, two operators are introduced.

The first one is the Hadamard product, which is denoted with the dot symbol $(\cdot)$. Given two matrices $\mathbf{A}$ and $\mathbf{B}$, it is defined as:

$$(\mathbf{A} \cdot \mathbf{B})_{ij} = (\mathbf{A})_{ij} \, (\mathbf{B})_{ij} \tag{53}$$

This operation is essentially the element-wise product of the elements composing the two matrices $\mathbf{A}$ and $\mathbf{B}$. The operation is defined if $\mathbf{A}$ and $\mathbf{B}$ share the same dimensions.

The second operation is the row-wise Kronecker product, indicated here with the symbol $\otimes_{\mathrm{r}}$. Given two matrices $\mathbf{A}$ and $\mathbf{B}$ with same number of rows and whose dimensions are $M \times N$ and $M \times S$, respectively, the operation is defined as:

$$\mathbf{A} \otimes_{\mathrm{r}} \mathbf{B} = \begin{bmatrix} A_{11}\mathbf{b}_1^{\mathrm{T}} & \dots & A_{1N}\mathbf{b}_1^{\mathrm{T}} \\ \vdots & \ddots & \vdots \\ A_{M1}\mathbf{b}_M^{\mathrm{T}} & \dots & A_{MN}\mathbf{b}_M^{\mathrm{T}} \end{bmatrix} \qquad \text{with: } \mathbf{b}_i = \{B_{i1},\, B_{i2},\, \dots\, B_{iS}\}^{\mathrm{T}} \tag{54}$$

B. Numerical Integration

The evaluation of the matrices of Eq. (46) requires surface integral to be performed. With this purpose, a background mesh is created, and each element is associated with e set of N_x and N_y integration points along the x and y directions, defined by the vectors $\mathbf{x}^{\mathrm{ip}} = \left\{x_1^{\mathrm{ip}} \dots x_{N_x}^{\mathrm{ip}}\right\}^{\mathrm{T}}$ and $\mathbf{y}^{\mathrm{ip}} = \left\{y_1^{\mathrm{ip}} \dots y_{N_y}^{\mathrm{ip}}\right\}^{\mathrm{T}}$. The corresponding weights of the quadrature rule

are collected into the vectors $\mathbf{w}^x$ and $\mathbf{w}^y$, which are combined as:

$$\mathbf{w} = \mathbf{w}^x \otimes \mathbf{w}^y = \left\{ w_1^x w_1^y,\ w_1^x w_2^y,\ \dots\ w_1^x w_{N_y}^y,\ w_2^x w_1^y,\ w_2^x w_2^y,\ \dots\ w_2^x w_{N_y}^y\ \dots,\ w_{N_x}^x w_1^y,\ w_{N_x}^x w_2^y,\ \dots\ w_{N_x}^x w_{N_y}^y \right\}^{\mathrm{T}} \tag{55}$$

to obtain a column vector of dimension $N_x N_y$ collecting the integration weights.

Following the same sorting operated in Eq. (55), the coefficients expressing the laminate constitutive law are organized into column vectors, each entry representing the evaluation of the corresponding elastic coefficient at a given integration point. For instance, the vector $\mathbf{A}_{11}$ collects the evaluation of the membrane stiffness term A_{11} at the various integration points, and is organized as:

$$\mathbf{A}_{11} = \left\{ A_{11}(x_1^{\mathrm{ip}}, y_1^{\mathrm{ip}}),\ A_{11}(x_1^{\mathrm{ip}}, y_2^{\mathrm{ip}}),\ \dots,\ A_{11}(x_{N_x}^{\mathrm{ip}}, y_{N_y}^{\mathrm{ip}}) \right\}^{\mathrm{T}} \tag{56}$$

This organization of data is operated for all the coefficients belonging to the matrices $\mathbf{A}$, $\mathbf{B}$, $\mathbf{D}$, $\mathbf{A}^{\mathrm{s}}$ defining the laminate constitutive law and appearing in Eq. (28). For future developments, it is useful to define the Hadamard product between the quadrature weights and the elastic coefficients:

$$\begin{aligned} \hat{\mathbf{A}}_{ik} &= \mathbf{w} \cdot \mathbf{A}_{ik} \qquad \hat{\mathbf{B}}_{ik} = \mathbf{w} \cdot \mathbf{B}_{ik}, \\ \hat{\mathbf{D}}_{ik} &= \mathbf{w} \cdot \mathbf{D}_{ik}, \quad \hat{\mathbf{A}}_{ik}^{\mathrm{s}} = \mathbf{w} \cdot \mathbf{A}_{ik}^{\mathrm{s}} \end{aligned} \tag{57}$$

Accordingly, the boundary functions ω_{u_k}, ω_{φ_α} and their derivatives are organized into column vectors expressing their evaluation at the integration points. For instance:

$$\boldsymbol{\omega}_{u_k} = \left\{ \omega_{u_k}(x_1^{\mathrm{ip}}, y_1^{\mathrm{ip}}),\ \omega_{u_k}(x_1^{\mathrm{ip}}, y_2^{\mathrm{ip}}),\ \dots,\ \omega_{u_k}(x_{N_x}^{\mathrm{ip}}, y_{N_y}^{\mathrm{ip}}) \right\}^{\mathrm{T}} \tag{58}$$

The last step regards the evaluation of the polynomial expansion and its derivatives at the integration points.

$$\boldsymbol{\mathcal{N}}^{\alpha\beta} = \begin{bmatrix} \mathbf{N}^{\alpha\beta}(x_1^{\mathrm{ip}}, y_1^{\mathrm{ip}}) \\ \vdots \\ \mathbf{N}^{\alpha\beta}(x_{N_x}^{\mathrm{ip}}, y_{N_y}^{\mathrm{ip}}) \end{bmatrix} = \begin{bmatrix} N_1^{\alpha\beta}(x_1^{\mathrm{ip}}, y_1^{\mathrm{ip}}) & \dots & N_{RS}(x_1^{\mathrm{ip}}, y_1^{\mathrm{ip}}) \\ \vdots & \ddots & \vdots \\ N_1(x_{N_x}^{\mathrm{ip}}, y_{N_y}^{\mathrm{ip}}) & \dots & N_{RS}(x_{N_x}^{\mathrm{ip}}, y_{N_y}^{\mathrm{ip}}) \end{bmatrix} \quad \text{with: } \alpha, \beta = \{0,\ 1\} \tag{59}$$

which is a matrix of dimensions $\left(N_x N_y\right) \times (RS)$.

Given the quadratic nature of the functional of Eq. (26), it is useful to define a matrix collecting the evaluation of the

products between the trial functions. In particular, the matrix is defined as:

$$\boldsymbol{\mathcal{M}}^{\alpha\beta\delta\gamma} = \boldsymbol{\mathcal{N}}^{\alpha\beta} \otimes_r \boldsymbol{\mathcal{N}}^{\delta\gamma} \quad \text{with: } \alpha, \beta, \delta, \gamma = \{0,\ 1\} \tag{60}$$

whose dimensions are $\left(N_x N_y\right) \times (RSRS)$. The matrix of Eq. (60) is computed just once and is then stored in memory.

The stiffness and mass matrices are:

$$\mathbf{K} = \begin{bmatrix} \mathbf{K}_{\mathrm{m}} & \mathbf{K}_{\mathrm{mb}} \\ \mathbf{K}_{\mathrm{mb}}^{\mathrm{T}} & \mathbf{K}_{\mathrm{b}} \end{bmatrix}, \quad \mathbf{M} = \begin{bmatrix} \mathbf{M}_{\mathrm{m}} & \mathbf{M}_{\mathrm{mb}} \\ \mathbf{M}_{\mathrm{mb}}^{\mathrm{T}} & \mathbf{M}_{\mathrm{b}} \end{bmatrix} \tag{61}$$

where the sub-blocks are:

$$\mathbf{K}_{\mathrm{m}} = \begin{bmatrix} \mathbf{K}^{u_x u_x} & \mathbf{K}^{u_x u_y} \\ & \mathbf{K}^{u_y u_y} \end{bmatrix}, \quad \mathbf{K}_{\mathrm{mb}} = \begin{bmatrix} \mathbf{0} & \mathbf{K}^{u_x \varphi_x} & \mathbf{K}^{u_x \varphi_y} \\ \mathbf{0} & \mathbf{K}^{u_y \varphi_x} & \mathbf{K}^{u_y \varphi_y} \end{bmatrix}, \quad \mathbf{K}_{\mathrm{b}} = \begin{bmatrix} \mathbf{K}^{u_z u_z} & \mathbf{K}^{u_z \varphi_x} & \mathbf{K}^{u_z \varphi_y} \\ & \mathbf{K}^{\varphi_x \varphi_x} & \mathbf{K}^{\varphi_x \varphi_y} \\ & & \mathbf{K}^{\varphi_y \varphi_y} \end{bmatrix} \tag{62}$$

$$\mathbf{M}_{\mathrm{m}} = \begin{bmatrix} \mathbf{M}^{u_x u_x} & \mathbf{0} \\ & \mathbf{M}^{u_y u_y} \end{bmatrix}, \quad \mathbf{M}_{\mathrm{mb}} = \begin{bmatrix} \mathbf{0} & \mathbf{M}^{u_x \varphi_x} & \mathbf{0} \\ \mathbf{0} & \mathbf{0} & \mathbf{M}^{u_y \varphi_y} \end{bmatrix}, \quad \mathbf{M}_{\mathrm{b}} = \begin{bmatrix} \mathbf{M}^{u_z u_z} & \mathbf{0} & \mathbf{0} \\ & \mathbf{M}^{\varphi_x \varphi_x} & \mathbf{0} \\ & & \mathbf{M}^{\varphi_y \varphi_y} \end{bmatrix} \tag{63}$$

And, in turn, the sub-blocks of the matrices $\mathbf{K}_{\mathrm{b}}$ and $\mathbf{M}_{\mathrm{b}}$ are:

$$\begin{aligned} K_{(mn)(rs)}^{u_z u_z} = \Bigg[& \left(\hat{\mathbf{A}}_{55} \cdot \boldsymbol{\omega}_{u_z,x}^2 + 2\hat{\mathbf{A}}_{45} \cdot \boldsymbol{\omega}_{u_z,x} \cdot \boldsymbol{\omega}_{u_z,y} + \hat{\mathbf{A}}_{44} \cdot \boldsymbol{\omega}_{u_z,y}^2 \right)^{\mathrm{T}} \boldsymbol{\mathcal{M}}^{0000} + \\ & + \left(\hat{\mathbf{A}}_{45} \cdot \boldsymbol{\omega}_{u_z} \cdot \boldsymbol{\omega}_{u_z,y} + \hat{\mathbf{A}}_{55} \cdot \boldsymbol{\omega}_{u_z} \cdot \boldsymbol{\omega}_{u_z,x} \right)^{\mathrm{T}} \left(\boldsymbol{\mathcal{M}}^{0010} + \boldsymbol{\mathcal{M}}^{1000} \right) + \\ & + \left(\hat{\mathbf{A}}_{44} \cdot \boldsymbol{\omega}_{u_z} \cdot \boldsymbol{\omega}_{u_z,y} + \hat{\mathbf{A}}_{45} \cdot \boldsymbol{\omega}_{u_z} \cdot \boldsymbol{\omega}_{u_z,x} \right)^{\mathrm{T}} \left(\boldsymbol{\mathcal{M}}^{0001} + \boldsymbol{\mathcal{M}}^{0100} \right) + \\ & + \left(\hat{\mathbf{A}}_{55} \cdot \boldsymbol{\omega}_{u_z}^2 \right)^{\mathrm{T}} \boldsymbol{\mathcal{M}}^{1010} + \left(\hat{\mathbf{A}}_{44} \cdot \boldsymbol{\omega}_{u_z}^2 \right)^{\mathrm{T}} \boldsymbol{\mathcal{M}}^{0101} + \left(\hat{\mathbf{A}}_{45} \cdot \boldsymbol{\omega}_{u_z}^2 \right)^{\mathrm{T}} \left(\boldsymbol{\mathcal{M}}^{1001} + \boldsymbol{\mathcal{M}}^{0110} \right) \Bigg] J \end{aligned} \tag{64}$$

$$\begin{aligned} K_{(mn)(rs)}^{u_z \varphi_x} = \Bigg[& \left(\hat{\mathbf{A}}_{45} \cdot \boldsymbol{\omega}_{\varphi_x} \cdot \boldsymbol{\omega}_{u_z,y} + \hat{\mathbf{A}}_{55} \cdot \boldsymbol{\omega}_{\varphi_x} \cdot \boldsymbol{\omega}_{u_z,x} \right)^{\mathrm{T}} \boldsymbol{\mathcal{M}}^{0000} + \left(\hat{\mathbf{A}}_{55} \cdot \boldsymbol{\omega}_{u_z} \cdot \boldsymbol{\omega}_{\varphi_x} \right)^{\mathrm{T}} \boldsymbol{\mathcal{M}}^{1000} + \\ & + \left(\hat{\mathbf{A}}_{45} \cdot \boldsymbol{\omega}_{u_z} \cdot \boldsymbol{\omega}_{\varphi_x} \right)^{\mathrm{T}} \boldsymbol{\mathcal{M}}^{0100} \Bigg] J \end{aligned} \tag{65}$$

$$K^{u_z\varphi_y}_{(mn)(rs)} = \left[\left(\hat{\mathbf{A}}_{44}\cdot\boldsymbol{\omega}_{\varphi_y}\cdot\boldsymbol{\omega}_{u_z,y} + \hat{\mathbf{A}}_{45}\cdot\boldsymbol{\omega}_{\varphi_y}\cdot\boldsymbol{\omega}_{u_z,x}\right)^{\mathrm{T}}\boldsymbol{\mathcal{M}}^{0000} + \left(\hat{\mathbf{A}}_{45}\cdot\boldsymbol{\omega}_{u_z}\cdot\boldsymbol{\omega}_{\varphi_y}\right)^{\mathrm{T}}\boldsymbol{\mathcal{M}}^{1000} + \right.$$
$$\left. + \left(\hat{\mathbf{A}}_{44}\cdot\boldsymbol{\omega}_{u_z}\cdot\boldsymbol{\omega}_{\varphi_y}\right)^{\mathrm{T}}\boldsymbol{\mathcal{M}}^{0100}\right] J \tag{66}$$

$$K^{\varphi_x\varphi_x}_{(mn)(rs)} = \left[\left(\hat{\mathbf{A}}_{55}\cdot\boldsymbol{\omega}^2_{\varphi_x} + \hat{\mathbf{D}}_{11}\cdot\boldsymbol{\omega}^2_{\varphi_x,x} + 2\cdot\hat{\mathbf{D}}_{16}\cdot\boldsymbol{\omega}_{\varphi_x,x}\cdot\boldsymbol{\omega}_{\varphi_x,y} + \hat{\mathbf{D}}_{66}\cdot\boldsymbol{\omega}^2_{\varphi_x,y}\right)^{\mathrm{T}}\boldsymbol{\mathcal{M}}^{0000} + \right.$$
$$+ \left(\hat{\mathbf{D}}_{11}\cdot\boldsymbol{\omega}_{\varphi_x}\cdot\boldsymbol{\omega}_{\varphi_x,x} + \hat{\mathbf{D}}_{16}\cdot\boldsymbol{\omega}_{\varphi_x}\cdot\boldsymbol{\omega}_{\varphi_x,y}\right)^{\mathrm{T}}\left(\boldsymbol{\mathcal{M}}^{0010} + \boldsymbol{\mathcal{M}}^{1000}\right) +$$
$$+ \left(\hat{\mathbf{D}}_{16}\cdot\boldsymbol{\omega}_{\varphi_x}\cdot\boldsymbol{\omega}_{\varphi_x,x} + \hat{\mathbf{D}}_{66}\cdot\boldsymbol{\omega}_{\varphi_x}\cdot\boldsymbol{\omega}_{\varphi_x,y}\right)^{\mathrm{T}}\left(\boldsymbol{\mathcal{M}}^{0001} + \boldsymbol{\mathcal{M}}^{0100}\right) +$$
$$\left. + \left(\hat{\mathbf{D}}_{16}\cdot\boldsymbol{\omega}^2_{\varphi_x}\right)^{\mathrm{T}}\left(\boldsymbol{\mathcal{M}}^{1001} + \boldsymbol{\mathcal{M}}^{0110}\right) + \left(\hat{\mathbf{D}}_{11}\cdot\boldsymbol{\omega}^2_{\varphi_x}\right)^{\mathrm{T}}\boldsymbol{\mathcal{M}}^{1010} + \left(\hat{\mathbf{D}}_{66}\cdot\boldsymbol{\omega}^2_{\varphi_x}\right)^{\mathrm{T}}\boldsymbol{\mathcal{M}}^{0101}\right] J \tag{67}$$

$$K^{\varphi_x\varphi_y}_{(mn)(rs)} = \left[\left(\hat{\mathbf{A}}_{45}\cdot\boldsymbol{\omega}_{\varphi_x}\cdot\boldsymbol{\omega}_{\varphi_y} + \hat{\mathbf{D}}_{12}\cdot\boldsymbol{\omega}_{\varphi_x,x}\cdot\boldsymbol{\omega}_{\varphi_y,y} + \hat{\mathbf{D}}_{16}\cdot\boldsymbol{\omega}_{\varphi_x,x}\cdot\boldsymbol{\omega}_{\varphi_y,x} + \hat{\mathbf{D}}_{26}\cdot\boldsymbol{\omega}_{\varphi_x,y}\cdot\boldsymbol{\omega}_{\varphi_y,y} + \hat{\mathbf{D}}_{66}\cdot\boldsymbol{\omega}_{\varphi_x,y}\cdot\boldsymbol{\omega}_{\varphi_y,x}\right)^{\mathrm{T}}\boldsymbol{\mathcal{M}}^{0000} + \right.$$
$$+ \left(\hat{\mathbf{D}}_{16}\cdot\boldsymbol{\omega}_{\varphi_y}\cdot\boldsymbol{\omega}_{\varphi_x,x} + \hat{\mathbf{D}}_{66}\cdot\boldsymbol{\omega}_{\varphi_y}\cdot\boldsymbol{\omega}_{\varphi_x,y}\right)^{\mathrm{T}}\boldsymbol{\mathcal{M}}^{0010} + \left(\hat{\mathbf{D}}_{12}\cdot\boldsymbol{\omega}_{\varphi_y}\cdot\boldsymbol{\omega}_{\varphi_x,x} + \hat{\mathbf{D}}_{26}\cdot\boldsymbol{\omega}_{\varphi_y}\cdot\boldsymbol{\omega}_{\varphi_x,y}\right)^{\mathrm{T}}\boldsymbol{\mathcal{M}}^{0001} +$$
$$+ \left(\hat{\mathbf{D}}_{12}\cdot\boldsymbol{\omega}_{\varphi_x}\cdot\boldsymbol{\omega}_{\varphi_y,y} + \hat{\mathbf{D}}_{16}\cdot\boldsymbol{\omega}_{\varphi_x}\cdot\boldsymbol{\omega}_{\varphi_y,x}\right)^{\mathrm{T}}\boldsymbol{\mathcal{M}}^{1000} + \left(\hat{\mathbf{D}}_{16}\cdot\boldsymbol{\omega}_{\varphi_x}\cdot\boldsymbol{\omega}_{\varphi_y}\right)^{\mathrm{T}}\boldsymbol{\mathcal{M}}^{1010} + \left(\hat{\mathbf{D}}_{12}\cdot\boldsymbol{\omega}_{\varphi_x}\cdot\boldsymbol{\omega}_{\varphi_y}\right)^{\mathrm{T}}\boldsymbol{\mathcal{M}}^{1001} +$$
$$\left. + \left(\hat{\mathbf{D}}_{26}\cdot\boldsymbol{\omega}_{\varphi_x}\cdot\boldsymbol{\omega}_{\varphi_y,y} + \hat{\mathbf{D}}_{66}\cdot\boldsymbol{\omega}_{\varphi_x}\cdot\boldsymbol{\omega}_{\varphi_y,x}\right)^{\mathrm{T}}\boldsymbol{\mathcal{M}}^{0100} + \left(\hat{\mathbf{D}}_{66}\cdot\boldsymbol{\omega}_{\varphi_x}\cdot\boldsymbol{\omega}_{\varphi_y}\right)^{\mathrm{T}}\boldsymbol{\mathcal{M}}^{0110} + \left(\hat{\mathbf{D}}_{26}\cdot\boldsymbol{\omega}_{\varphi_x}\cdot\boldsymbol{\omega}_{\varphi_y}\right)^{\mathrm{T}}\boldsymbol{\mathcal{M}}^{0101}\right] J \tag{68}$$

$$K^{\varphi_y\varphi_y}_{(mn)(rs)} = \left[\left(\hat{\mathbf{A}}_{44}\cdot\boldsymbol{\omega}^2_{\varphi_y} + \hat{\mathbf{D}}_{66}\cdot\boldsymbol{\omega}^2_{\varphi_y,x} + 2\cdot\hat{\mathbf{D}}_{26}\cdot\boldsymbol{\omega}_{\varphi_y,x}\cdot\boldsymbol{\omega}_{\varphi_y,y} + \hat{\mathbf{D}}_{22}\cdot\boldsymbol{\omega}^2_{\varphi_y,y}\right)^{\mathrm{T}}\boldsymbol{\mathcal{M}}^{0000} + \right.$$
$$+ \left(\hat{\mathbf{D}}_{26}\cdot\boldsymbol{\omega}_{\varphi_y}\cdot\boldsymbol{\omega}_{\varphi_y,y} + \hat{\mathbf{D}}_{66}\cdot\boldsymbol{\omega}_{\varphi_y}\cdot\boldsymbol{\omega}_{\varphi_y,x}\right)^{\mathrm{T}}\left(\boldsymbol{\mathcal{M}}^{0010} + \boldsymbol{\mathcal{M}}^{1000}\right) +$$
$$+ \left(\hat{\mathbf{D}}_{22}\cdot\boldsymbol{\omega}_{\varphi_y}\cdot\boldsymbol{\omega}_{\varphi_y,y} + \hat{\mathbf{D}}_{26}\cdot\boldsymbol{\omega}_{\varphi_y}\cdot\boldsymbol{\omega}_{\varphi_y,x}\right)^{\mathrm{T}}\left(\boldsymbol{\mathcal{M}}^{0001} + \boldsymbol{\mathcal{M}}^{0100}\right) +$$
$$\left. + \left(\hat{\mathbf{D}}_{26}\cdot\boldsymbol{\omega}^2_{\varphi_y}\right)^{\mathrm{T}}\left(\boldsymbol{\mathcal{M}}^{1001} + \boldsymbol{\mathcal{M}}^{0110}\right) + \left(\hat{\mathbf{D}}_{22}\cdot\boldsymbol{\omega}^2_{\varphi_y}\right)^{\mathrm{T}}\boldsymbol{\mathcal{M}}^{0101} + \left(\hat{\mathbf{D}}_{66}\cdot\boldsymbol{\omega}^2_{\varphi_y}\right)^{\mathrm{T}}\boldsymbol{\mathcal{M}}^{1010}\right] J \tag{69}$$

$$M^{u_zu_z}_{(mn)(rs)} = I_0\left(\mathbf{w}\cdot\boldsymbol{\omega}^2_{u_z}\right)^{\mathrm{T}}\boldsymbol{\mathcal{M}}^{0000}J \tag{70}$$

$$M^{\varphi_x\varphi_x}_{(mn)(rs)} = I_2\left(\mathbf{w}\cdot\boldsymbol{\omega}^2_{\varphi_x}\right)^{\mathrm{T}}\boldsymbol{\mathcal{M}}^{0000}J \tag{71}$$

$$M^{\varphi_y\varphi_y}_{(mn)(rs)} = I_2\left(\mathbf{w}\cdot\boldsymbol{\omega}^2_{\varphi_y}\right)^{\mathrm{T}}\boldsymbol{\mathcal{M}}^{0000}J \tag{72}$$

where J is the Jacobian of the transformation between the element of the background mesh and the reference element in natural coordinates, i.e.:

$$J = \frac{l_x l_y}{4} \tag{73}$$

The other terms appearing in Eqs. (62) and (63) are obtained similarly and are not reported here for the sake of brevity.

Funding Sources

The author would like to thank Ministero dell'Istruzione, dell'Università e della Ricerca for funding this research under PRIN 2017 program.

References

[1] Arbocz, J., and Hol, J., "Shell stability analysis in a computer aided engineering (CAE) environment," 34^{th} *AIAA/ASME/ASCE/AHS/ASC Structures, Structural Dynamics and Material Conference*, La Jolla, CA, 1993, pp. 300–314.
https://doi.org/10.2514/6.1993-1333

[2] Arbocz, J., Hol, J., and de Vries, J., "The effect of initial imperfections on shell stability," *Modern Problems of Structural Stability*, Springer, 2002, pp. 117–228.
https://doi.org/10.1007/978-3-7091-2560-1_4

[3] Bisagni, C., and Vescovini, R., "Analytical formulation for local buckling and post-buckling analysis of stiffened laminated panels," *Thin-Walled Structures*, Vol. 47, No. 3, 2009, pp. 318–334.
https://doi.org/10.1016/j.tws.2008.07.006

[4] Bisagni, C., and Vescovini, R., "Fast tool for buckling analysis and optimization of stiffened panels," *Journal of Aircraft*, Vol. 46, No. 6, 2009, pp. 2041–2053.
https://doi.org/10.2514/1.43396

[5] Vescovini, R., and Bisagni, C., "Buckling analysis and optimization of stiffened composite flat and curved panels," *AIAA Journal*, Vol. 50, No. 4, 2012, pp. 904–915.
https://doi.org/10.2514/1.J051356

[6] Hyer, M., and Charette, R., "Use of curvilinear fiber format in composite structure design," 30^{th} *AIAA Structures, Structural Dynamics, and Materials Conference*, Mobile, AL, 1989, pp. 2137–2145.
https://doi.org/10.2514/3.10697

[7] Olmedo, R., and Gürdal, Z., "Buckling response of laminates with spatially varying fiber orientations," 34^{th}*AIAA/ASME/ASCE/AHS/ASC Structures, Structural Dynamics and Material Conference*, La Jolla, CA, 1993, pp.

2261–2269.
https://doi.org/10.2514/6.1993-1567

[8] Gürdal, Z., and Olmedo, R., "In-plane response of laminates with spatially varying fiber orientations-variable stiffness concept," *AIAA Journal*, Vol. 31, No. 4, 1993, pp. 751–758.
https://doi.org/10.2514/3.11613

[9] Gürdal, Z., Tatting, B., and Wu, C., "Variable stiffness composite panels: effects of stiffness variation on the in-plane and buckling response," *Composites Part A: Applied Science and Manufacturing*, Vol. 39, No. 5, 2008, pp. 911–922.
https://doi.org/10.1016/j.compositesa.2007.11.015

[10] Coburn, B., and Weaver, P., "Buckling analysis, design and optimisation of variable stiffness sandwich panels," *20^{th} International Conference on Composite Materials*, Copenhagen, 2015, pp. 1–12.

[11] Vescovini, R., and Dozio, L., "A variable-kinematic model for variable stiffness plates: Vibration and buckling analysis," *Composite Structures*, Vol. 142, 2016, pp. 15–26.
https://doi.org/10.1016/j.compstruct.2016.01.068

[12] Oliveri, V., Milazzo, A., and Weaver, P., "Thermo-mechanical post-buckling analysis of variable angle tow composite plate assemblies," *Composite Structures*, Vol. 183, 2018, pp. 620–635.
https://doi.org/10.1016/j.compstruct.2017.07.050

[13] Sciascia, G., Oliveri, V., Milazzo, A., and Weaver, P., "Ritz solution for transient analysis of variable-stiffness shell structures," *AIAA Journal*, Vol. 58, No. 4, 2020, pp. 1796–1810.
https://doi.org/10.2514/1.J058686

[14] Vescovini, R., Spigarolo, E., Jansen, E., and Dozio, L., "Efficient post-buckling analysis of variable-stiffness plates using a perturbation approach," *Thin-Walled Structures*, Vol. 143, 2019, p. 106211.
https://doi.org/10.1016/j.tws.2019.106211

[15] Zhao, W., and Kapania, R., "Prestressed vibration of stiffened variable-angle tow laminated plates," *AIAA Journal*, 2019, pp. 1–19.
https://doi.org/10.2514/1.J057719

[16] Pagani, A., and Sanchez-Majano, A., "Influence of fiber misalignments on buckling performance of variable stiffness composites using layerwise models and random fields," *Mechanics of Advanced Materials and Structures*, 2020, pp. 1–16.
https://doi.org/10.1080/15376494.2020.1771485

[17] Janssens, T., and Castro, S., "Semi-analytical modelling of variable stiffness laminates with cut-outs," *AIAA Scitech 2021 Forum*, Virtual, 2021, pp. 1–18.
https://doi.org/10.2514/6.2021-0440

[18] Kurpa, L., Pilgun, G., and Amabili, M., "Nonlinear vibrations of shallow shells with complex boundary: R-functions method and experiments," *Journal of Sound and Vibration*, Vol. 306, No. 3-5, 2007, pp. 580–600.
https://doi.org/10.1016/j.jsv.2007.05.045

[19] Waberski, A., "Vibration statistics of thin plates with complex form," *AIAA Journal*, Vol. 16, No. 8, 1978, pp. 788–794.
https://doi.org/10.2514/3.7582

[20] Avramov, K., Tyshkovets, O., and Maksymenko-Sheyko, K., "Analysis of nonlinear free vibration of circular plates with cut-outs using R-function method," *Journal of Vibration and Acoustics*, Vol. 132, No. 5, 2010, pp. 1–1.
https://doi.org/10.1115/1.4001496

[21] Kurpa, L., Rvachev, V., and Ventsel, E., "The R-function method for the free vibration analysis of thin orthotropic plates of arbitrary shape," *Journal of Sound and Vibration*, Vol. 261, No. 1, 2003, pp. 109–122.
https://doi.org/10.1016/S0022-460X(02)00946-X

[22] Rvachev, V., and Sheiko, T., "R-functions in boundary value problems in mechanics," *Applied Mechanics Reviewes*, Vol. 48, No. 4, 1995, pp. 151–188.
https://doi.org/10.1115/1.3005099

[23] Rvachev, V., Sheiko, T., and Shapiro, V., "The R-function method in boundary-value problems with geometric and physical symmetry," *Journal of Mathematical Sciences*, Vol. 97, No. 1, 1999, pp. 3888–3899.
https://doi.org/10.1007/BF02364929

[24] Shapiro, V., "Theory of R-functions and applications: a primer," Technical report 91-1291, Department of Computer Science, Cornell University, 1991.

[25] Amabili, M., *Nonlinear Vibrations and Stability of Shells and Plates*, Cambridge University Press, 2008.
https://doi.org/10.1017/CBO9780511619694

[26] Reddy, J., *Mechanics of Laminated Composite Plates and Shells: Theory and Analysis*, CRC Press, Boca Raton, 2004.
https://doi.org/10.1201/b12409

[27] Carrera, E., "A class of two-dimensional theories for anisotropic multilayered plates analysis," *Atti Accademia delle Scienze di Torino. Memorie Scienze Fisiche*, Vol. 19, 1995, pp. 1–39.

[28] Demasi, L., "∞^6 mixed plate theories based on the Generalized Unified Formulation. Part I: Governing equations," *Composite Structures*, Vol. 87, No. 1, 2009, pp. 1–1.
https://doi.org/10.1016/j.compstruct.2008.07.013

[29] D'Ottavio, M., "A Sublaminate Generalized Unified Formulation for the analysis of composite structures," *Composite Structures*, Vol. 142, 2016, pp. 187–199.
https://doi.org/10.1016/j.compstruct.2016.01.087

[30] Alhajahmad, A., Abdalla, M., and Gürdal, Z., "Design tailoring for pressure pillowing using tow-placed steered fibers," *Journal of Aircraft*, Vol. 45, No. 2, 2008, pp. 630–640.
https://doi.org/10.2514/1.32676

[31] Coburn, B., "Buckling of stiffened variable stiffness panels," Ph.D. Thesis, University of Bristol, 2015.

[32] Wu, Z., Weaver, P., Raju, G., and Kim, B., "Buckling analysis and optimisation of variable angle tow composite plates," *Thin-Walled Structures*, Vol. 60, 2012, pp. 163–172.
https://doi.org/10.1016/j.tws.2012.07.008

[33] Vescovini, R., Oliveri, V., Pizzi, D., Dozio, L., and Weaver, P., "A semi-analytical approach for the analysis of variable-stiffness panels with curvilinear stiffeners," *International Journal of Solids and Structures*, Vol. 188-189, 2020, pp. 244–260.
https://doi.org/10.1016/j.ijsolstr.2019.10.011

[34] Hyer, M., *Stress Analysis of Fiber-Reinforced Composite Materials*, McGraw-Hill, New York, 1998.

[35] Reddy, J., *Energy Principles and Variational Methods in Applied Mechanics*, John Wiley and Sons, New York, USA, 1984.

[36] Vescovini, R., Dozio, L., D'Ottavio, M., and Polit, O., "On the application of the Ritz method to free vibration and buckling analysis of highly anisotropic plates," *Composite Structures*, Vol. 192, 2018, pp. 460–474.
https://doi.org/10.1016/j.compstruct.2018.03.017

[37] Liu, G., and Gu, Y., *An Introduction to Meshfree Methods and Their Programming*, Springer, Dordrecht, The Netherlands, 2005.
https://doi.org/10.1007/1-4020-3468-7

[38] Akhavan, H., and Ribeiro, P., "Natural modes of vibration of variable stiffness composite laminates with curvilinear fibers," *Composite Structures*, Vol. 93, No. 11, 2011, pp. 3040–3047.
https://doi.org/10.1016/j.compstruct.2011.04.027